

Effect of edge trimming parameters on surface quality of carbon fiber reinforced polymer composites (CFRP): Taguchi Method

S.A. Sundi^{1,2,*}, R. Izamshah², M.S. Kasim², M.F. Jaafar², N. Syuhada Nasir¹, M.H. Hassan³

¹Fakulti Teknologi Kejuruteraan Mekanikal dan Pembuatan, Universiti Teknikal Malaysia Melaka, Hang Tuah Jaya, 76100 Durian Tunggal, Melaka, Malaysia

²Fakulti Kejuruteraan Pembuatan, Universiti Teknikal Malaysia Melaka, Hang Tuah Jaya, 76100 Durian Tunggal, Melaka, Malaysia

³School of Mechanical Engineering, Universiti Sains Malaysia, 14300 Nibong Tebal, Pulau Pinang, Malaysia

*Corresponding e-mail: syahrul.azwan@utem.edu.my

Keywords: Edge trimming; CFRP; surface roughness; Taguchi method

ABSTRACT – The main objective of this research was to investigate the effect of machining parameters towards surface quality during edge trimming process on a specific Carbon Fiber Reinforced Polymer (CFRP). The machining parameters focused in this work were namely cutting speed (V_c) and feed per tooth (f_z). The CFRP panel used is measured 3.25 mm in thickness with 28 number of plies in total. Burr tool geometry made of uncoated tungsten carbide diameter of 6.35 mm was used to perform the edge trimming process. Taguchi method is adopted to plan the overall experimental. Mitutoyo Surftest SJ-410 has been utilized to measure the surface roughness value. From ANOVA analysis, both studied factors proven to be the significant factors towards the surface quality of the trimmed surface. Details results elaborated and discussed further in this paper.

1. INTRODUCTION

Machining composite materials is hard to be performed due to the mechanical, thermal properties and the high abrasiveness of the reinforcement constituents. In manufacturing of aero-structural composite material, milling and drilling are critical for finishing trimmed edges of panels or making accurate holes to rivet pieces together. The behavior of composite such as its inhomogeneity and interaction with the cutting tool whilst machining is a complex phenomenon to be understood [1]. Gara and Tsoumarev [2] discovered that the transverse roughness does not depend on cutting conditions, it depends only on tool geometry. Contrary to the longitudinal roughness which was not only depending on the tool geometry but also the cutting conditions. Feed per tooth was found to be the highest statistical and physical influence on the surface roughness for knurled or burr tool. Meanwhile, Sundi et al. [3] summarized that spindle speed was found to be the main influential factor towards surface finish in edge trimming a specific CFRP material. In different research experimented by Duboust et al. [4] proved that surface roughness increased with machining distance. They also concluded that diamond coated tool with multiple cutting teeth (burr tool) was able to produce a good quality surface although at high feed rate in comparison with polycrystalline diamond (PCD) tool. Statistical methods obtained indicate that the feed rate and tool type had the most significant effect on the surface quality.

2. METHODOLOGY

The CFRP panel measured 3.25 mm in thickness and the type of fabric was unidirectional (UD). It has 28 number of plies in total which consist of 2 thin layer of glass/epoxy woven fabrics 0.08 mm at the top and bottom of the CFRP laminate play the role of protecting the outer surfaces of the panel. The stacking sequence was [45/135/90₂/0/90/0/90/0/135/45₂/135]. The nominal fiber volume fraction was 60%.

The type cutting tool used was router or burr tool made of tungsten carbide (uncoated) and diameter 6.35mm (refer Figure 1). The machine utilized in this work was a Hass CNC Gantry Router – 3 Axis GR-510. Down milling has been selected as the mode of machining configuration. Total travel distance of each run was 260 mm. In this study, the edge trimming process performed with 100% of tool diameter or step width (a_e) and the depth of cut (a_p) was taken in full thickness of the selected composite panel. This is to replicate the actual industrial practice done by composite manufacturers.



Figure 1 Geometrical feature of router or burrs tool.

There were two machining parameters focused namely cutting speed (V_c) and feed per tooth (f_z). The range of cutting speeds applied were of 50 m/min (low), 100 m/min (moderate), and 150 m/min (high) speed whilst for feed per tooth; 0.05, 0.1, and 0.15 mm/rev. Table 1 represents the machining parameters applied in this work. Taguchi method (Orthogonal Array L9) one of the statistical techniques was adopted to plan the overall experiment.

Surface roughness tester; Surftest SJ-410 manufactured by Mitutoyo (Figure 2) is used to measure the surface finish of the workpiece. In this study, R_a (Arithmetical mean deviation) is referred to measure the surface roughness. Longitudinal surface roughness is evaluated with the stylus travel distance set at 4 mm on each measurement. There were 5 points of measurement taken on every machined surface and final average R_a is obtained to represent the result of surface finish on every specimen (Table 2).

Table 1 Machining parameters.

| Run (R) | Cutting Speed, V_c | RPM | Feed per Tooth, F_z (mm/rev) | V_f mm/min |
|---------|----------------------|------|--------------------------------|--------------|
| 1 | 50 | 2506 | 0.05 | 125 |
| 2 | 100 | 5012 | 0.15 | 752 |
| 3 | 50 | 2506 | 0.1 | 251 |
| 4 | 100 | 5012 | 0.05 | 251 |
| 5 | 100 | 5012 | 0.1 | 501 |
| 6 | 150 | 7518 | 0.1 | 752 |
| 7 | 150 | 7518 | 0.05 | 376 |
| 8 | 50 | 2506 | 0.15 | 376 |
| 9 | 150 | 7518 | 0.15 | 1128 |

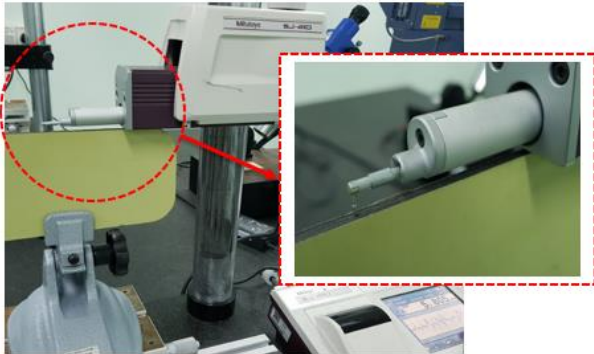


Figure 2 Surface roughness measurement by SJ-410.

3. RESULTS AND DISCUSSION

Analysis of Variance (ANOVA) was carried out to determine which factor or machining parameter namely cutting speed, V_c and feed per tooth, F_z significantly affect the performance characteristics or selected response namely surface roughness.

Table 2 Overall result of surface roughness, Ra

| Run | 1 | 2 | 3 | 4 | 5 | Avg. |
|-----|-------|-------|-------|-------|-------|-------|
| 1 | 1.95 | 1.28 | 0.94 | 2.80 | 1.11 | 1.62 |
| 2 | 7.57 | 7.79 | 6.50 | 9.35 | 2.44 | 6.73 |
| 3 | 4.59 | 4.14 | 2.43 | 2.43 | 2.63 | 3.25 |
| 4 | 2.50 | 2.46 | 2.42 | 2.95 | 3.06 | 2.68 |
| 5 | 2.80 | 3.92 | 8.09 | 6.98 | 4.59 | 5.28 |
| 6 | 7.43 | 7.55 | 9.23 | 7.45 | 8.89 | 8.11 |
| 7 | 2.30 | 3.66 | 3.93 | 3.97 | 4.34 | 3.64 |
| 8 | 6.07 | 5.33 | 5.98 | 6.41 | 6.77 | 6.11 |
| 9 | 15.72 | 13.33 | 10.68 | 13.33 | 10.03 | 12.62 |

Tables 3 illustrates the result of ANOVA analysis for the average Ra values during edge trimming of a specific CFRP chosen in this study. This analysis was computed for a level of confidence of 95 %. The Model F-value (in bold) from Table 3 shows 10.800 which implies the model is significant. There is only a 2.03% chance that a "Model F-Value" this large could occur due to noise. Thus, both factors; A = cutting speed and B = feed per tooth have significant effect to the chosen response; surface finish. Meanwhile, Figure 3 exhibits a 3D bar graph which summarized the effect of both factors; cutting speed and feed per tooth towards the surface quality of the trimmed surface. Lower cutting speed and feed per tooth are preferred to obtain the minimized surface roughness.

Table 3 ANOVA Result for surface roughness.

| Source | SOS | df | Square | Mean value | Prob > F |
|------------------|--------|----|--------|------------|----------|
| Model | 83.492 | 4 | 20.873 | 10.800 | 0.0203 |
| A-Cutting Speed | 31.120 | 2 | 15.560 | 8.0511 | 0.0396 |
| B-Feed per Tooth | 52.372 | 2 | 26.186 | 13.550 | 0.0165 |
| Residual | 7.7304 | 4 | 1.9326 | | |
| Cor Total | 91.222 | 8 | | | |

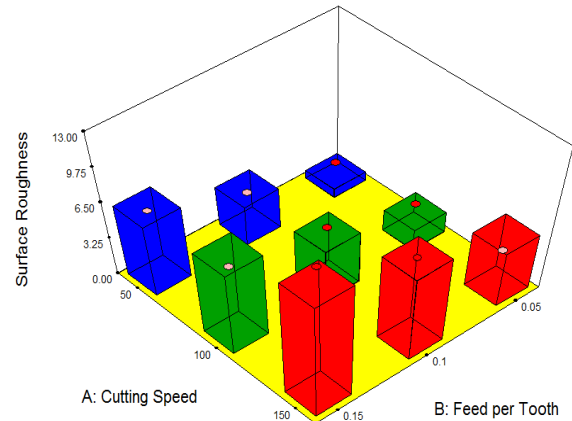


Figure 3 3D bar graph illustrates the effect of cutting speed and feed per tooth towards surface roughness.

4. CONCLUSION

This paper presented an evidence on the effect of machining parameters namely cutting speed and feed rate towards the edge trimmed surface quality of a specific CFRP material according to the result obtained by ANOVA analysis.

ACKNOWLEDGEMENT

Authors would like to thank Ministry of Education Malaysia for their financial support. (FRGS/2018/FKP-AMC/F00378).

REFERENCES

- [1] Sheikh-Ahmad, J. Y. (2009). *Machining of polymer composites* (Vol. 387355391). New York: Springer.
- [2] Gara, S., & Tsoumarev, O. (2016). Effect of tool geometry on surface roughness in slotting of CFRP. *The International Journal of Advanced Manufacturing Technology*, 86(1-4), 451-461.
- [3] Sundi, S. A., Izamshah, R., Kasim, M. S., & Abdullah, M. K. A. (2019, January). Effect of machining parameters on surface quality during edge trimming of multi-directional CFRP material: Taguchi method. In *IOP Conference Series: Materials Science and Engineering* (Vol. 469, No. 1, p. 012095). IOP Publishing.
- [4] Duboust, N., Melis, D., Pinna, C., Ghadbeigi, H., Collis, A., Ayvar-Soberanis, S., & Kerrigan, K. (2016). Machining of carbon fibre: optical surface damage characterisation and tool wear study. *Procedia CIRP*, 45, 71-74.

Optimization of treated SN 0W20 grade engine oil enhance with hBN nanoparticles

Muhammad Ilman Hakimi Chua Abdullah^{1,2,*}, Mohd Redzuan Jamil¹, Mohd Fadzli Bin Abdollah^{2,3}

¹Fakulti Teknologi Kejuruteraan Mekanikal dan Pembuatan, Universiti Teknikal Malaysia Melaka, Hang Tuah Jaya, 76100 Durian Tunggal, Melaka, Malaysia

²Centre for Advanced Research on Energy, Universiti Teknikal Malaysia Melaka, Hang Tuah Jaya, 76100 Durian Tunggal, Melaka, Malaysia

³Fakulti Kejuruteraan Mekanikal, Universiti Teknikal Malaysia Melaka, Hang Tuah Jaya, 76100 Durian Tunggal, Melaka, Malaysia

*Corresponding e-mail: ilmanhakimi@utem.edu.my

Keywords: SN 0W20; hBN; friction

ABSTRACT – The purpose of this study is to determine the optimal design parameters in obtaining the lowest coefficient of friction (COF) and wear by hexagonal boron nitride (hBN) nanoparticles, dispersed in fully synthetic engine oil (SN 0W20). L9 orthogonal arrays was constructed using the Taguchi method to determine the parameter contribution. Four-ball tester is used for conducting tribological testing according to ASTM standard D4172. By referring to the analysis of S/N ratio, COF and wear scar was reduced significantly with addition hBN nanoparticles into the treated engine oil SN 0W20. As conclusion hBN nanoparticles able to be the next future additive for oil manufacturer.

1. INTRODUCTION

Nowadays, the demand of new lubricant is highly undoubtedly due to the diverse application that keeps on increasing. It is a must for producing new lubricant to meet future demand. Most of current lubricants are derived from the crude oil which is not adaptable to the environment because of its toxicity and non-biodegradability. The waste oil can be threatening to the world if it is not handled correctly. The recycling and regeneration of waste oil can be an alternative way to prevent pollution by treated the waste oil.

Recently, numerous studies have been conducted on how to improve engine oil by enhancing with nanoparticles. Nanoparticles are particles that have a size normally around 100 nanometers or less. It possesses better characteristics through its size, shape, hardness and the weight percentage of usage. Unlike any lubricant additives, nanoparticles are readily good at entering contact asperities, thermal stability, a variety of particle chemistries, and reaction rate with the surface without an induction period, which is important for conventional [1,2]. Over the past decades, researcher has stated the addition of nanoparticles such as copper (Cu), titanium oxide (TiO₂), and aluminium oxide (Al₂O₃) to lubricant is effective on decreasing wear and friction [3,4].

Capable of hBN nanoparticle as an additive in conventional engine oil already been widely study but several successful studies not yet been discovered for treated engine oil. Therefore, this study mainly focuses on the capability of hBN as a new additive with suitable homogenized parameter on the tribological properties for treated SN 0W20 engine oil.

2. EXPERIMENTAL SETUP

The samples composition was prepared according to Table 1 and Table 2 shows the L9 orthogonal arrays for testing condition.

Table1 Sample preparation.

| Types of nanoparticles | Concentration of nanoparticles | Vol.% SN-0W20 | Concentration of surfactant agent (oleic acid) |
|-------------------------------|--------------------------------|---------------|--|
| Hexagonal boron nitride (hBN) | 0.5 vol% (1.15 g) | 9.2 | 0.3 vol% |
| | 0.05vol% (0.115 g) | 99.65 | |
| | 0.1vol % (0.23 g) | 99.6 | |

Table 2. L9 Orthogonal arrays Taguchi Method

| Level | Parameter | | |
|-------|--------------|------------|------------------|
| | hBN (vol .%) | Time (min) | Temperature (°C) |
| 1 | 0.05 | 10 | 40 |
| 2 | 0.05 | 20 | 60 |
| 3 | 0.05 | 30 | 80 |
| 4 | 0.1 | 10 | 60 |
| 5 | 0.1 | 20 | 80 |
| 6 | 0.1 | 30 | 40 |
| 7 | 0.5 | 10 | 80 |
| 8 | 0.5 | 20 | 60 |
| 9 | 0.5 | 30 | 40 |

Tribological testing was performed to identify the coefficient of friction (COF) and wear rate accordance to ASTM D 4172 followed by scanning electron microscope (SEM). The parameters setup was 1200 rpm, 392.4 N, 3600 sec, and 75°C, respectively. Within the four-ball tester, three 12.7 mm diameter carbon-chrome steel balls were clamped together and covered with lubricant for evaluation. Fourth steel ball (of the same diameter), referred to as the top ball, was held in a special collet inside a spindle and rotated by an AC motor. The top ball was rotated in contact with the three fixed balls, which were immersed in the sample oil.

3. RESULTS AND DISCUSSION

According to the S/N ratios analysis shows by Figure 1, the optimal parameter obtained was 0.1 vol.% of hBN nanoparticles composition that heated at 40°C for 30 minutes. Based on the result, homogenized time and temperature show a significant contribution in obtaining the lowest friction and wear.

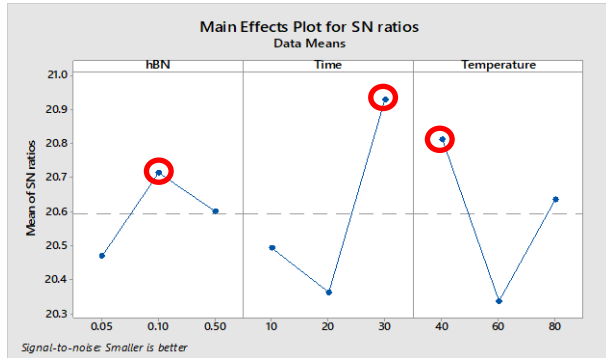


Figure 1 Main effects plot for S/N ratios.

The optimal parameters enhance the tribological property of the sample with a characteristic of low coefficient of friction and wear rate. Based on the result, the longest time exposure during the homogenization process improves the stability of the nanoparticles between the oil molecules [5], beside the control temperature help to reduce the lubricity changes while samples were prepared. This was the advantages of sonification process for dispersed the nanoparticles. Figure 2 shows the CoF result obtained for all the tested sample which show the optimal result give the lowest CoF value indicated by sample 6. Figure 3 shows the wear scar diameter for all tested samples. Sample of optimized parameter obtained the smallest WSD which is 404 μm compared to sample 5 which are the smaller WSD obtained by L9 Orthogonal arrays samples with 631.5 μm and the worse is retained by sample 8 with 643.2 μm .

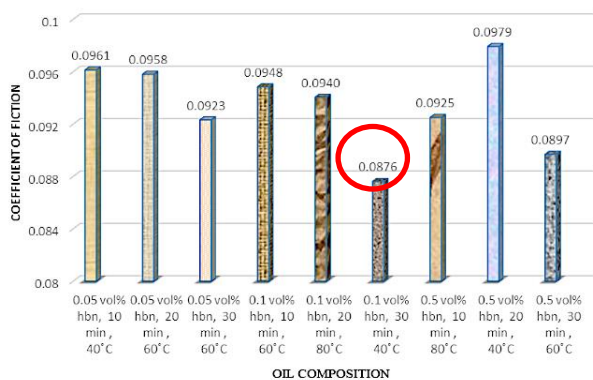


Figure 2 Average CoF value obtained for tested samples.

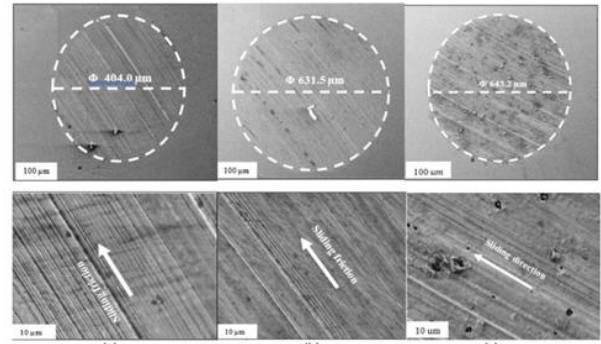


Figure 3 Wear Scar Diameter for sample (a) optimized parameter, (b) sample 5 and (c) sample 8.

4. CONCLUSION

The optimal parameter for obtaining the lowest CoF and WSD is given by 0.1 vol.% of hBN nanoparticles composition that heated at 40°C for 30 minutes. Homogenized time and temperature play a significant effect in obtaining the lowest CoF and WSD. Further investigation may help in term of developing solid proved for future nanoparticles as and promising additives in treated SN 0W20 engine oil.

ACKNOWLEDGEMENT

The author would like to thank Universiti Teknikal Malaysia Melaka and Ministry of Education Malaysia for funding this research under Fundamentals Grant Scheme (FRGS/2018/FTKMP-CARE/F00385).

REFERENCES

- [1] Abdullah, M. I. H. C., Abdollah, M. F. B., Amiruddin, H., Tamaldin, N., Nuri, N. R. M., Masjuki, H., & Rafeq, S. A. (2014). Improving engine oil properties by dispersion of hBN/Al₂O₃ nanoparticles. *Applied Mechanics and Materials*, 607, 70-73.
- [2] Shahnazar, S., Bagheri, S., & Hamid, S. B. (2016). Enhancing lubricant properties by nanoparticle additives. *International Journal of Hydrogen Energy*, 41(4), 3153-3170.
- [3] Guzman, B. F. L., Ribeiro, O. S. J., Seabra, M. L., & Kalab, L. A. J. (2018). Experimental investigation of the tribological behavior of lubricants with additive containing copper nanoparticles. *Tribology International*, 117, 52-58.
- [4] Nanthagopal, K., Ashok, B., Tamilarasu, A., Johny, A., & Mohan, A. (2017). Influence on the effect of zinc oxide and titanium dioxide nanoparticles as an additive with Calophyllum inophyllum methyl ester in a CI engine. *Energy Conversion and Management*, 146, 8-19.
- [5] Mohd Nawi, A. E., Abdullah, M. I. H. C., & Abdollah, M. F. B. (2018). Dispersion stability of hBN nanoparticle in liquid phase with different dispersion agents. *Journal of Mechanical Engineering*, 15(2), 143-153.

Characterization of aluminium oxide composites

Sunil Pathak^{1,*}, Balmukund Dhakar²

¹⁾ Faculty of Engineering Technology, Universiti Malaysia Pahang, Lebuhraya Tun Razak
26300 Gambang, Kuantan, Pahang, Malaysia

²⁾ Department of Mechanical Engineering, Shri G. S. Institute of Technology and Science Indore, 452003, India

*Corresponding e-mail: sunilpathak@ump.edu.my; sunilpathak87@gmail.com

Keywords: Alumina; hardness; roughness

ABSTRACT - Three alumina-based composites were fabricated by die compaction followed by sintering. The porous microstructure was analyzed by SEM (Scanning Electron Microscopy) and EDS (Energy Dispersive X-Ray). In order to know the variation in surface roughness parameters (R_a , R_z , R_{max}) of alumina composites the surface roughness of the samples was measured using a three-dimensional laser surface roughness analyzer. The microhardness values of the composites were evaluated using Vickers microhardness tester.

1. INTRODUCTION

In general, the average mechanical properties of alumina composite increase with the increase in alumina composition [1,2]. The bonding of the particles of alumina composite prepared by compaction improves by sintering process. The sintering process starts with the powdered form. The powder of particles is poured into the feed ram. The feed ram moves across the die opening and deposits the alumina powder into the die. The compression ram compresses part is ejected out of the die. The feed ram then moves the compressed part away. The compressed part is placed in oven and heated to a very high temperature which further fuses and sinter, the metal into totally solid form. The part is allowed to cool slowly. The work focuses to study and investigate the morphology of the Al_2O_3 composites through Scanning Electron Microscope (SEM) SEM (Scanning Electron Microscopy) and EDS (Energy Dispersive X-Ray). In order to know the variation in surface roughness parameters (R_a , R_z , R_{max}) of alumina composites the surface roughness, this research also aims to study the microhardness of the composites.

2. METHODOLOGY

α -alumina powder was used as a raw material. The nomenclature of the samples is shown in Table 1. The alumina powders were consolidated into compacts by pressing un-axially at 30 MPa. The pellets were sintered at 1350°C, 1500°C and 1600°C for 2h soaking time. The surface roughness of the samples has been measured using a laser three dimensional Surface roughness analyzer (COMS, EMS2002 AD-3D 100XY, Japan). The surface roughness profile was obtained using EMS2002AD-3D program. The R_a , R_z and R_{max} values of each surface were obtained by taking the average of five profiles. The microstructures of the sintered samples have been observed by using a scanning electron microscope (SEM: JEOL, JSM 5600 LV, Japan). It equipped with energy dispersive spectroscopy (EDC,

Oxford Link ISIS 300). The surface and cross-sections were polished by using silicon carbide papers. The related SEM pictures were then processed by image analysis (ImageJ) software to observe the porosity level and pores distribution. Microhardness measurement was carried out by using a Vickers micro indenter (VMHT MOT, Leica Microsystems, Wetzlar, Germany). The indentations were performed at a load of 9.84 N for a dwell time of 15 s.

Table 1 Nomenclature of the samples.

| Alumina % composition | Name |
|-----------------------|------|
| 86.54 | A |
| 93.37 | B |
| 84.94 | C |

3. RESULTS AND DISCUSSION

3.1 Microstructure

As shown in Figures 1, 2 and 3 the cross-section of the sintering alumina exhibits a typical porous microstructure, characterized by pores with different sizes. The formation of an amorphous phase at lesser extent as displayed in Figure 1, the alumina powder is composed of fused and crushed particles with blocky and angular morphology. Figure 2 shows some pores, microcracks (denoted by black arrows) embedded in microstructure. By analyzing the cross-sectional SEM microstructure in Figure 3 it can be seen that the alumina coating exhibits a lamellar and relatively dense microstructure and pores with different sizes.

3.2 Surface Roughness

The variation in surface roughness has been studied by analyzing the variation in surface roughness parameters R_a , R_z and R_{max} of various surfaces at different composition of alumina. Table 2 presents the detailed results of the surface roughness values in all the three selected samples. The variation in R_a value for the coating samples were obtained by consolidation using different percentage of alumina. R_a value for sample A is 3.82 μm , sample B is 10.58 μm and sample C is 1.22 μm . Sample B possesses the highest surface roughness due to the high composition of alumina. There is least difference in R_a for sample A and sample C as the composition of alumina differences is not really significant. This may be due to effective migration of surface grains during the sintering process. Lesser difference in R_z is observed for the sample A and sample C. For the sample A, R_z values show that the roughness is 2.94 μm and for the sample C is 0.933 μm compared to sample B it reached 4.43 μm . It

can also be observed that there was a dramatic change in R_z value for sample B when the huge amount of alumina was used for the compaction. For the samples, R_{max} value of 3.827, 10.588 and 1.226 is observed while consolidated using different percentage of alumina, respectively.

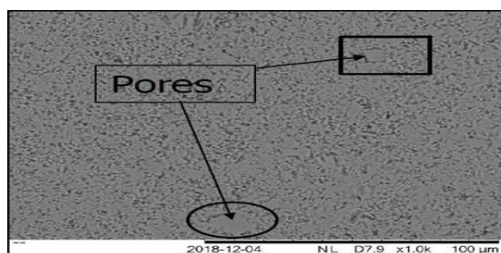


Figure 1 Micrographs of sample A i.e. 86.54% alumina.

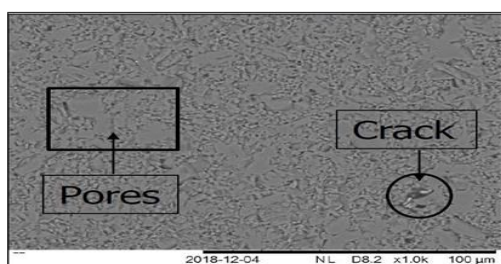


Figure 2 Micrographs of sample B i.e. 93.37% of alumina.

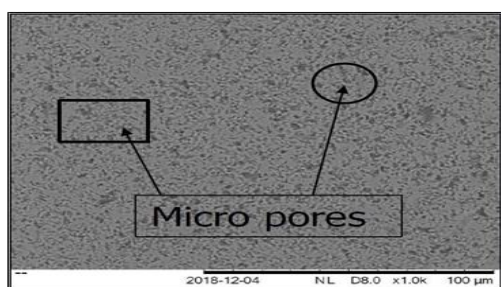


Figure 3 Micrographs of sample C i.e. 84.94% of alumina.

Table 2 Roughness values of the different samples.

| Roughness values from 9 different locations | | R_a (μm) | R_z (μm) | R_{max} (μm) |
|---|---------|-------------------------|-------------------------|-----------------------------|
| Sample A | Average | 0.374 | 2.945 | 3.827 |
| | SD | 0.0239 | 0.245 | 0.720 |
| Sample B | Average | 0.457 | 4.435 | 10.588 |
| | SD | 0.321 | 2.162 | 6.426 |
| Sample C | Average | 0.0962 | 0.926 | 1.226 |
| | SD | 0.0151 | 0.258 | 0.442 |

3.3 Microhardness

Table 3 presents the microhardness of the samples. The hardness of the surface of components is an important property affecting their tribological performance. Variations in hardness of alumina composite containing 86.54%, 93.37% and 84.94% weight fractions of Al_2O_3 are shown in Table 3. Vickers microhardness of the composite is 1878.82, 1981.94 and 1905.8 HV for the composite containing 86.54%, 93.37% and 84.94% of Al_2O_3 respectively. The average hardness increased due to the increase in 37.763% and 37.819% of

Al_2O_3 weight fraction respectively. It is believed that due to high hardness of Al_2O_3 and stronger interfacial bonding between particulates at higher sintering temperature, the improvement in the hardness of the ceramic coatings occurred. However, the value of the hardness for all the compositions is although different in number but all the materials are considered possessing same hardness. This is because the value of hardness is measured in the range and if there is small difference in value, the material is not considered as difference in hardness.

Table 3 Microhardness of the different samples.

| SAMPLE | A | B | C |
|--|---------|---------|---------|
| Hardness values from 5 different locations in HV | 1748.9 | 1977.2 | 2204.9 |
| | 1748.9 | 1921.9 | 1658.5 |
| | 1689.9 | 2158.2 | 1621.9 |
| | 2253.2 | 1961.1 | 2121.8 |
| Average (HV) | 1953.2 | 1891.3 | 1921.9 |
| | 1878.82 | 1981.94 | 1905.8 |
| SD | 231.917 | 104.097 | 263.691 |

4. CONCLUSION

The microstructure of the alumina composite C is the best from the other sample because the amount/quantity of the porous is less as compared to other samples. If the process happened at the optimum level the structure will be more systematic and the bonding between the particles is stronger because there will be no space for the porous between the atomic or elements structure.

Attempts have been made to study the variation in the roughness parameters when the alumina percentage is different. It is important to make compacts with the least alumina compositions to the roughness of the surface to analyze a homogeneous uniform microstructure. The roughness values found high in the sample where alumina percentage is more [3].

Hardness of the alumina-based composite depend on alumina percentage as can be seen from sample B which has the highest hardness value and contain maximum amount of alumina ceramics [4,5]. However, the least differences in percentage of alumina in case of sample A and C, the result still showing there is insignificant difference in the hardness value. It can be said that the alumina powder that possessing in the composite affected the surface hardness of the materials significantly.

ACKNOWLEDGEMENT

Authors thank Universiti Malaysia Pahang for the funding provided to conduct this research through Research Grant (RDU1703113).

REFERENCES

- [1] Pathak, S., & Saha, G. (2017). Development of sustainable cold spray coatings and 3D additive manufacturing components for repair/manufacturing applications: a critical review. *Coatings*, 7(8), 122.
- [2] Dhakar, B., Chatterjee, S., & Sabiruddin, K. (2017). Phase stabilization of plasma-sprayed alumina coatings by spraying mechanically blended

- alumina–chromia powders. *Materials and Manufacturing Processes*, 32(4), 355-364.
- [3] Dhakar, B., Chatterjee, S., & Sabiruddin, K. (2017). Measuring mechanical properties of plasma-sprayed alumina coatings by nanoindentation technique. *Materials Science and Technology*, 33(3), 285-293.
- [4] Dhakar, B., Chatterjee, S., & Sabiruddin, K. (2017). Influence of process parameters on the formation of phases and mechanical properties of plasma sprayed Al₂O₃–Cr₂O₃ coatings. *Materials research innovations*, 21(6), 367-376.
- [5] Dhakar, B. M., Dwivedi, D. K., & Sharma, S. P. (2012). Studies on remelting of tungsten carbide and rare earth modified nickel base alloy composite coating. *Surface engineering*, 28(1), 73-80.

Friction and wear mechanisms of palm kernel activated carbon polymer composite by Raman spectroscopy study

Dayang Nor Fatin Mahmud¹, Hilmi Amiruddin^{1,2}, Mohd Fadzli Bin Abdollah^{1,2,*}, Nor Azmmi Bin Masripan^{1,2}, Mohd Rody Bin Mohamad Zin^{1,2}, Noreffendy Tamaldin^{1,2}

¹) Fakulti Kejuruteraan Mekanikal, Universiti Teknikal Malaysia Melaka, Hang Tuah Jaya, 76100 Durian Tunggal, Melaka, Malaysia

²) Centre for Advanced Research on Energy, Universiti Teknikal Malaysia Melaka, Hang Tuah Jaya, 76100 Durian Tunggal, Melaka, Malaysia

*Corresponding e-mail: mohdfadzli@utem.edu.my

Keywords: Palm kernel activated carbon; polymer; friction; wear; Raman spectroscopy

ABSTRACT – The objective of this paper is to investigate the friction and wear mechanisms of palm kernel activated carbon (PKAC) polymer composite by Raman spectroscopy study. A ball-on-disc tribometer was used to conduct the dry sliding test at different degree of contact pressures with constant sliding speed, sliding distance and operating temperature. The results found that the coefficient of friction (COF) of the composite decreases with the contact pressure, though the wear rate remains at an almost constant value. Then, COF and wear rate increased drastically when exceeding a critical limit of 90MPa. Raman spectroscopy study reveals that phase transformation of PKAC polymer composite changed from a carbon-like-structure to a graphite-like-structure (sp²) on the top layer of the composite.

1. INTRODUCTION

At the present times, there is an encouraging emergence of alternative technologies such as thin bio/eco-materials, film coatings and green lubricants that were being used to offer a sustainable supply for the global need by reducing friction and wear of components or parts as a mean to save energy [1]. Malaysia is one of the biggest user and exporters of palm oil in the global arena. The palm oil industry produces a vast amount of waste comprising of around 90% of biomass waste and just around 10% of the palm oil. The utilization of agricultural waste as another composite material has additionally been observed to be inexhaustible and generally more affordable and at last could use the waste viably into riches. In this way, this propelled us to explore the capability of enacted carbon got from one of the biggest waste palm oils called activated carbon-epoxy composite derived from palm kernel be used as a new tribological material [2].

The activated carbon-epoxy composite derived from palm kernel also known as palm oil extraction waste materials, is composed of carbonaceous, highly porous adsorptive medium that has a similar atomic structure to that of graphite, but in a disorganised form. Furthermore, this activated carbon in the form of composite has high potential to be a self-lubricating material with a little friction coefficient and more durable wear resistance caused by the presence of the remaining natural oils in palm kernel [3].

There were few researches that describe the operating state effects on the features of activated carbon-epoxy composite tribology from the palm kernel, such as effect of composition, operating parameter and surface texture. Nevertheless, studies on effect of contact pressure and its mechanisms is still limited to explore the features of palm kernel activated carbon (PKAC) polymer composite. Therefore, the purpose of this study is to investigate the friction and wear mechanisms of palm kernel activated carbon (PKAC) polymer composite by Raman spectroscopy study at various contact pressures dry sliding conditions.

2. EXPERIMENTAL PROCEDURE

A disc with 74mm in diameter, 5mm thickness was produced by mixing 60 wt.% PKAC (250 µm particle size) with 40 wt.% epoxy, where the hardener to resin ratio is 1:4. The mixture was then put into a mould and pressed using a hot-press machine.

The dry sliding experiment was carried out utilising a ball-on-disc tribometer, in accordance with ASTM G99-05 (2016). All tests were performed at different applied contact pressure between 59.84 and 119.99MPa, with a 500rpm sliding speed at 3000 m of perpetual sliding distance. The operating temperature is 27°C. ASTM52100 (EN31) chrome steel ball, as a counter surface, with two different diameter sizes of 10mm and 12.7mm, was used in this study. Each of the test was then repeated for three times to lessen the errors in the experimental. The phase transformation of composite was analysed by adopting the UniRAM 3500 Raman spectroscopy. The physical-mechanical properties of both disc and ball are shown in Table 1.

Table 1 Physical-mechanical properties of the ball and disc materials before testing.

| Properties | ^a Disc | ^b Steel ball |
|--------------------------------------|-------------------|-------------------------|
| Hardness, H [GPa] | 8.36 | 7.45 |
| Young Modulus, E [GPa] | 7.61 | 210 |
| Poisson's ratio, ν | 0.23 | 0.3 |
| Density, ρ [g/cm ³] | 1.4 | 7.81 |
| Surface roughness, R_a [µm] | 0.4 | 0.022 |

^a Properties acquired from laboratory measurements.

^b Properties acquired from manufacturer.

3. RESULTS AND DISCUSSION

Figure 1 presents the data on coefficient of friction (COF) and the wear rate of PKAC polymer composite. It can be seen that at the beginning, COF decreases with contact pressure, though the wear rate remains at an almost constant value. This could imply that the transfer layer formation on the counter surfaces, could have accounted for the decreasing COF and wear rate due to the surface contact changes from carbonised-steel to carbonised-carbonised materials [4]. This phenomenon could also be deduced by the friction-induced phase

transformation; which will be discussed later. However, when the contact pressure increases to the critical limit of 90MPa, the COF and wear rate rose dramatically due to the deterioration of this transfer layer, thus forcing the counter surface of the protective layer to disappear. This also signifies that the contact surface has experienced high abrasion due to the ploughing between the contact surfaces, which might have influenced the increment of the friction force and wear rate, which led to removal of the material [5].

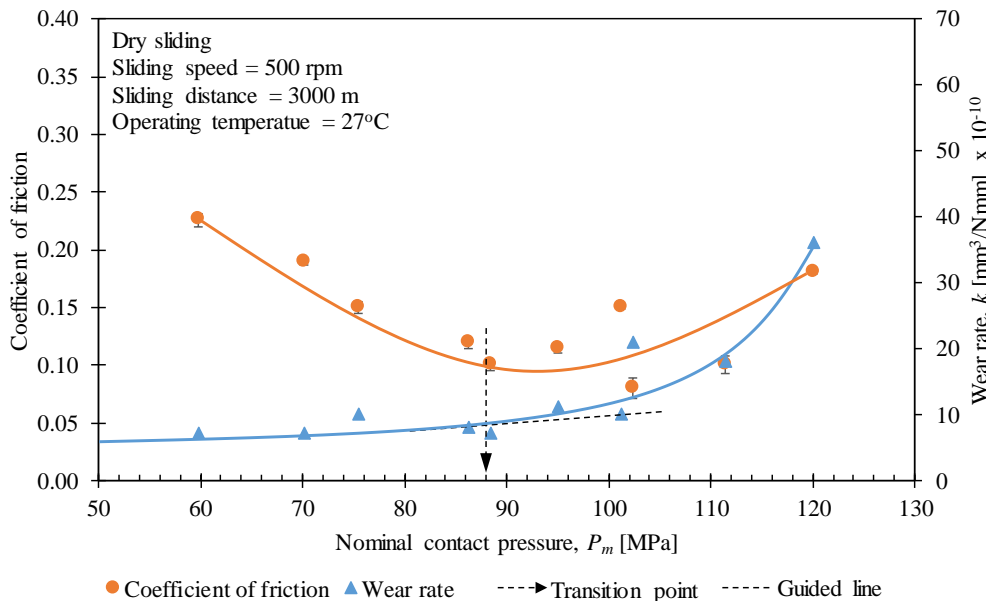


Figure 1 Effect of contact pressure on the coefficient of friction and wear rate of PKAC polymer composite.

Figure 2 presents typical Raman spectra obtained from the activated carbon derived of palm kernel epoxy disc composite before testing and from the wear track region after dry sliding test (500 rpm sliding speed). Based on this study, the composite bond structure, at atomic scale, was described with the ratio of intensity (I_D/I_G), G-shift and full-width at half maximum (FWHM) of G peak. From Figure 2, it shows that the G peak shifted to a higher frequency at 1583.87 cm^{-1} (G peak), compared to the composite before testing at 1577.76 cm^{-1} (G peak). While, the I_D/I_G ratio increased with contact pressure, accompanied by a narrowing of FWHM for the G peak, which correlated well to a higher sp^2 content [6]. Thus, the Raman spectra clearly show a change in the wear track surface structure from carbon-like to graphite-like structure.

4. CONCLUSION

In a dry sliding test, at the beginning when the value of contact pressure increase it can be seen that COF decreases, though the wear rate remains at an almost constant value. However, when the contact pressure exceeds a critical limit of 90MPa, the friction coefficient and the wear rate of PKAC polymer composite rapidly increased. Furthermore, from phase transformation study, the stability of friction and wear of disc composite is due to the changes of surface layer phase transformation.

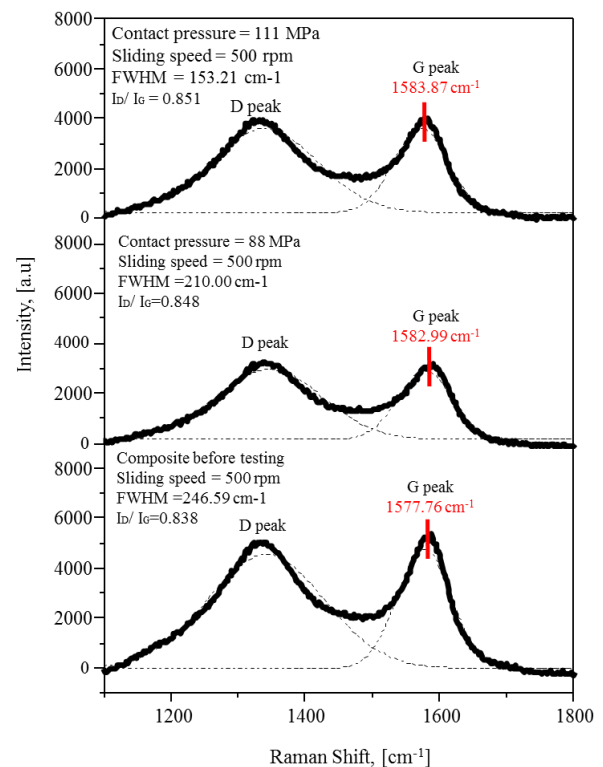


Figure 2 Raman spectra of the disc composite.

ACKNOWLEDGMENT

The project is supported by a grant from Universiti Teknikal Malaysia Melaka (Grant no.: PJP/2019/FKM(10A)/S01683).

REFERENCES

- [1] Abdollah, M. F. B., Yamaguchi, Y., Akao, T., Inayoshi, N., Tokoroyama, T., and Umehara, N., 2011. The effect of maximum normal impact load, absorbed energy, and contact impulse, on the impact crater volume/depth of DLC coating. *Tribology Online*, 6(6), pp. 257-264.
- [2] Lagel, M. C., Hai, L., Pizzi, A., Basso, M. C., Delmotte, L., Abdalla, S., Zahed, A., and Al-Marzouki, F.M., (2016). Automotive brake pads made with a bioresin matrix. *Industrial Crops and Products*, 85, pp. 372-381.
- [3] Yahya, M. A., Al-Qodah, Z., Ngah, C. Z., (2015). Agricultural bio-waste materials as potential sustainable precursors used for activated carbon production: A review. *Renewable and Sustainable Energy Reviews*, 46, 218-235.
- [4] Mahmud, D. N. F., Abdollah, M. F. B., Masripan, N. A. B., Tamaldin, N., & Amiruddin, H. (2019). Influence of contact pressure and sliding speed dependence on the tribological characteristics of an activated carbon-epoxy composite derived from palm kernel under dry sliding conditions. *Friction*, 7(3), pp. 227–236.
- [5] Chowdhury, M. A., and Helali, M. M., 2008. The effect of amplitude of vibration on the coefficient of friction for different materials. *Tribology International*, 41(4), pp. 307–14.
- [6] Jiu, J. T., Wang, H., Cao, C. B., Zhu, J. T., Jiu, H., Wang, C. B., and Cao Zhu, H. S., 1999. Effect of annealing temperature on the structure of diamond-like carbon films by electrodeposition technique. *Journal of Materials Science*, 34(21), pp. 5205-5209.

An Investigation of chip formation on different penetration angle for orthopaedic surgical bone drilling

M.S. Noorazizi^{1,2,*}, K.R. Jamaludin¹, S. Sarip¹, R. Izamshah², R. Zamri, L. Abdullah, M.N. Maslan²

¹) Fakulti Teknologi dan Informatik Razak, Universiti Teknologi Malaysia, Jalan Sultan Yahya Petra, 54100, Kuala Lumpur, Malaysia

²) Fakulti Kejuruteraan Pembuatan, Universiti Teknikal Malaysia Melaka, Hang Tuah Jaya, 76100 Durian Tunggal, Melaka, Malaysia

*Corresponding e-mail: noorazizi@utm.my

Keywords: Chips formation; bone drilling; hole quality

ABSTRACT – This work is to investigate the effects of chips formation type on the quality of bone drilling procedure. Totals of 17 drills were design and tested with different geometry namely point angle, helix angle and web thickness on different penetration angle (0° , 15° , and 30°) to mimic the manually control penetration by the surgeon. The results depict that variation in chip formation morphology depends on drills design geometry, drilling parameters and different penetration angle. The chip morphology physical shape in bone drilling in this experiment can be categorized as powder, needle, conical fan, short spiral fan and long conical fan with different size. It can be observed that penetration angle 0° and 15° give the small sizes chips morphology compared to 30° for all the drills design.

1. INTRODUCTION

One of the principal methods for repairing and reconstruction of a bone fracture are achieved by drilling the bone and fixing the separate parts together using screws, wires and plates. Many problems are encountered with the bone drilling process such as holes accuracy, drill wander and excessive heat generation which were directly related with the drilling parameter [1,4]. Many different drill-bit designs and geometries have been suggested over the years each with its own promising results [2-4]. However, most of the studies neglected the effects of penetration angle on the drilling performances. Generally, in normal orthopedic surgery, bone drilling is performed using hand drills and the penetration angles is greatly dependent on the surgeon's manual skill and are normally deviated from the normal axis. Hole quality in bone drilling is evaluated in terms of hole error diameter and cylindricity, surface roughness, and burr [1]. Equally important, drilling quality includes aperture deviation, migration and gradient of the aperture axis and the changes of surface geometry. In this paper knowledge between both drill geometrical parameter and drilling penetration angle on the chip formation will be identified.

2. EXPERIMENTAL WORK

In this experiment, AISI 420B stainless steel medical grade rod with diameter 4.3 mm were ground to form the drill bits with varying angles namely point angle, helix angle and web thickness as depicted in Table 1. Stainless steel drill bit exhibits good corrosion resistance and can minimize the tool wear effect. Totals

of 51 holes were drilled with 3 holes replication for each run. To eliminate the apparatus wear impact on the result, the apparatus was cleaned with a brush and wet tissue before each drilling process.

Table 1 Drill geometrical angles design level.

| | Name | Unit | Low | High |
|---|-------------------|----------|-----|------|
| A | Web Thickness | % | 14 | 32 |
| B | Point Angle | $^\circ$ | 90 | 140 |
| C | Helix Angle | $^\circ$ | 16 | 38 |
| D | Penetration Angle | $^\circ$ | 0 | 30 |

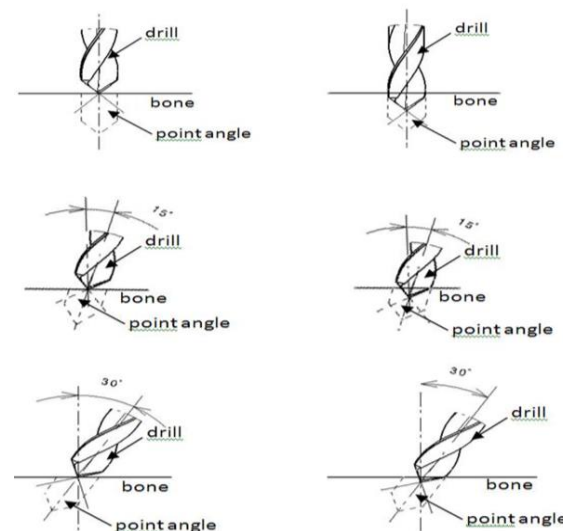


Figure 1 Drill bit position before entry and after 0° , 15° , and 30° penetration angles.

Bovine cortical femur bone was chosen as the work material due to its closeness properties and characteristics with human bone [3-5]. Fresh cortical (compact bone) samples are cuts and mills from bovine femur with a uniform thickness of 4 mm. The drilling tests were performed using a DMU60 monoBLOCK DECKEL MAHO CNC 5-Axis Machine. The drilling speed of 1000 rpm and 100 mm/min feed rate were employed to represent the actual manual surgical hand drills speed and surgeon penetration feed (0° , 15° , and 30°) as shown in Figure 1. Optical microscope (EMZ-Meiji) equipped with a digital camera was used for the analysis and observation of hole accuracy, burr and chip

formation. This optical microscope has a 93mm working distance with rotatable through 360° as shown in Figure 2.

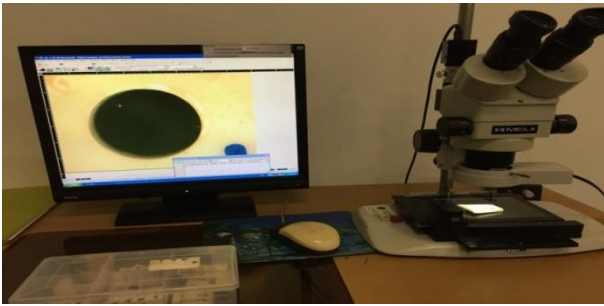


Figure 2 Optical microscope (EMZ-Meiji) equipped with digital camera.

3. RESULTS AND DISCUSSION

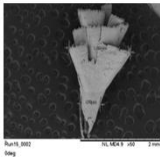
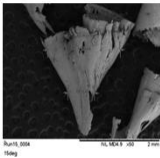
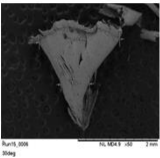
In this experiment, the chip formation was observed from the moment the drill lips touched the bone surface until the end of the hole. More importantly, it has two flutes to carry the chips up from the cutting edges to the top of the hole where they are cast off. From the observation, the bone chips were seen rotating along the drill bit rubbing against the hole's surface and blocking the flutes. The bone chips also impacted the hole wall surface which produced a bending moment in the chip leading to its fracture once the strain in the chip exceeded the critical value. In general, the chip morphology physical shape in bone drilling in this experiment can be categorized such as powder, needle, conical fan, short spiral fan and long conical fan as shown in Figure 3.



Figure 3 Chip shapes generated by drilling bone powder with needle and conical fan.

Some bone chip samples were taken to determine the chip morphology during bone drilling. The comparison bone chip shapes produce by different penetration mode were shown in Table 2.

Table 2 Comparison chip shapes produce by different penetration mode.

| Penetration | 0 | 15 | 30 |
|-------------|---|---|---|
| Morphology |  |  |  |
| Shape | Long spiral fan shape | Short spiral fan shape | Short conical fan shape |
| Size | 1.55mm | 1.82mm | 2.02mm |

From the results shape chip formation of sample 15 design drill bit (Web Thickness: 23%, Point Angle: 115° , Helix Angle: 27°) at 0° penetration angle. Macroscopic observations show that long spirals fan shape were built with the conical top size = 1.55mm and the down size = $478\mu\text{m}$. It is different as short spiral fan shape chip formation of at 15° penetration angle. The conical size of the chip is higher at the top = 1.82mm and down conical shape size = $670\mu\text{m}$. Meanwhile at 30° penetration angle from macroscopic observation shows that short conical fan shape was built with the conical top size = 2.02mm and the conical down size = $707\mu\text{m}$.

4. CONCLUSION

Hence, understanding the effects of drilling geometry parameter on the hole performances is important to provide the reference values for the development of high-performance surgical drill designs in orthopedic bone surgery application. It can be seen that drilling in the higher penetration angle slightly increased the size of chip shape compared to the 0° and 15° penetration angles.

ACKNOWLEDGEMENT

The authors wish to thank Universiti Teknologi Malaysia, Universiti Teknikal Malaysia Melaka, Hospital Angkatan Tentera Kem Terendak Melaka and the UTM RMC through Research University Grant Tier 2 for the technical and financial support for the experiment.

REFERENCES

- [1] Samsuddin, N. M., Izamshah, R., Kasim, M. S., & Haron, C. H. C. (2017). Evaluation of Hole Performance and Force Magnitude on Drilling Parameter for Orthopaedic Surgical Bone Drilling. *Journal of Mechanical Engineering*, (2), 37-47.
- [2] Pandey, R. K., & Panda, S. S. (2013). Drilling of bone: A comprehensive review. *Journal of clinical orthopaedics and trauma*, 4(1), 15-30.
- [3] Izamshah, R., Noorazizi, M. S., Kasim, M. S., & Haron, C. C. (2016, February). Influence of Orthopaedic Drilling Parameters on Surface Roughness and Cutting Force of Bone Drilling Process. In *International Conference on Electronics, Mechanics, Culture and Medicine*. Atlantis Press.
- [4] Hillery, M. T., & Shuaib, I. (1996). The Drilling of Bone Using Guide Wires and Twist Drills, MT Hillery, ed. In *Proceedings of the 13th Irish Manufacturing Conference (IMC-13)*, Limerick, Ireland, September (pp. 4-6).
- [5] Vashishth, D., Tanner, K. E., & Bonfield, W. (2000). Contribution, development and morphology of microcracking in cortical bone during crack propagation. *Journal of Biomechanics*, 33(9), 1169-1174.

Effect of single zincating duration on the properties of copper activated aluminium Alloy 7075 substrate

Intan Sharhida Othman^{1,*}, Marco Starink², Shun Chai Wang²

¹⁾ Fakulti Kejuruteraan Pembuatan, Universiti Teknikal Malaysia Melaka, Hang Tuah Jaya, 76100 Durian Tunggal, Melaka, Malaysia

²⁾ School of Engineering, University of Southampton, SO17 1BJ Southampton, United Kingdom

*Corresponding e-mail: intan_sharhida@utem.edu.my

Keywords: aluminium alloy 7075, nickel coating, copper activation, adhesion, zincating, electrodeposition

ABSTRACT – A combination of copper activation processing with various single zincating durations was applied on aluminium alloy 7075 (AA7075) substrate, in order to overcome the drawbacks of conventional single zincating. The evolution of surface morphology and surface composition during the zincating process at various durations were characterized by scanning electron microscopy (SEM) and energy dispersive x-rays analysis (EDX). The adhesion of the coating was investigated using a scratch tester. SEM result shows the uniformity of the zinc particles on the substrates was improved by increasing the single zincating duration. The adhesion of the composite coating was improved at longer zincating duration as compared to the conventional single zincating process. The morphology has contributed to the improvement of coating adhesion.

1. INTRODUCTION

Extensive research has been carried out in academia and in industry to find the most suitable and effective method of surface pre-treatment on aluminium alloys. The research included direct plating on aluminium alloys [1], a pre-electrodeposition process [2], zincating processes [3], zincating process with copper pre-treatment [4], and nickel striking [5]. Among these, the most satisfactory and practical method of surface pre-treatment process for plating on aluminium alloys is the zincate immersion treatment, which is known as zincating. Zincating treatment produces a zinc layer on the surface of the aluminium alloys, thus preventing the formation of aluminium oxide and providing adequate contact with any metal electroplated onto these alloys [6,7].

However, Azumi et al. [8] found a continuous dissolution of the aluminium alloys during the first and second zincating. The high dissolution reaction of the aluminium substrate in a concentrated alkaline zincating solution may lead to a serious damage of the substrate [9]. The dissolution of substrates and uniform distribution of zinc deposits can be improved by applying a copper pre-treatment before the zincating process [4, 8]. These copper deposit act as nucleation sites for zinc deposition during the zincating process and produce a uniform and dense layer of zinc deposits which almost completely cover the substrate [4].

To the best of our knowledge, the effects of combination of copper activation process with various single zincating duration on electrodeposited nickel coating on AA7075 substrate has not been reported.

Therefore, the objective of this paper is to improve the conventional single zincating process by extending the immersion duration of the copper activated substrate in zincating solution.

2. METHODOLOGY

The AA 7075 substrate was first immersed in an etching solution containing 0.5 M H₂SO₄ + 3.13 x 10⁻⁴ M CuSO₄ at room temperature for 10 minutes to achieve the copper activation process. The conventional single zincating process involves immersion of the substrate in the zincating solution for 1 minute and in this work, this was extended to 5, 15, 10 and 20 minutes. The current density used for the electrodeposition process was 4 A/dm² under direct current mode with the total time of electrodeposition set at one hour. The composition of the electrolyte is as follows: NiSO₄·6H₂O (200 g/l), NaCl (20 g/l), C₁₂H₂₅SO₄Na (0.2 g/l), C₇H₅NO₃S (3 g/l), H₃BO₃ (30 g/l) and 2-butyne-1,4-diol, C₄H₆O₂ (0.5 g/l). The zincating solution consists of ZnO (100 g/l), NaOH (525 g/l), FeCl (1 g/l) and KNaC₄H₄O₆·4H₂O (9.8 g/l). The coating adhesions were evaluated by scratch tester (Teer Coating, ST-3001) and the failures were then analyzed using optical microscopy (OM).

3. RESULTS AND DISCUSSION

3.1 Surface Morphology and Elemental

Composition of Copper Activated Substrate

From EDX analysis in the SEM, it was confirmed that bright particles which were deposited on the substrate after the copper activation process are copper (Figure 1).

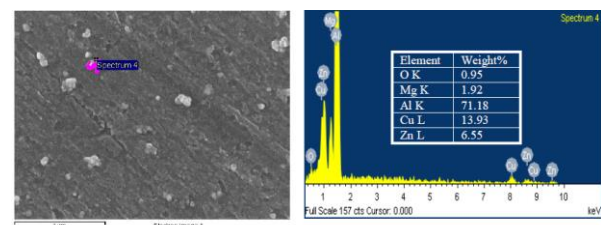


Figure 1 SEM micrograph and EDX analysis of copper activated AA7075 substrates at 10 minutes.

3.2 Effect of Single Zincating Duration on the Surface Morphology of Copper Activated Substrate

After 5 minutes of immersion in the zincating solution, growth of zinc nuclei was observed on the

surface (Figure 2(b)). As the duration increased to 10 minutes, the zinc particles became bigger and some agglomerations occurred (Figure 2(c)). After 15 minutes, the zinc particles were continuously growing and by 20 minutes, the zinc particles completely covered the surface (Figure 2(d,e)). It is apparent in the figure that a high density of zinc particles is occurs for the longer zincating duration studied.

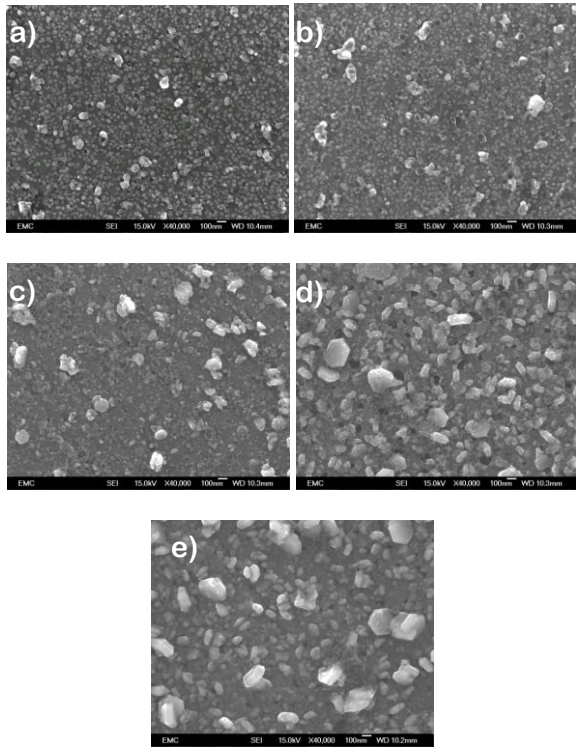


Figure 2 SEM micrographs of AA7075 substrates after various single zincating durations with copper activation, (a) 1, (b) 5, (c) 10, (d) 15 and (e) 20 minutes.

3.3 Effect of Single Zincating Durations on the Adhesion of Composite Coatings

As the progressive applied loads increased during the scratch test, more cracks were generated by the diamond stylus (Figure 3). The most striking result to emerge from the scratch testing is that only the sample which was produced from 1 minute of single zincating showed adhesive failure. The coating was ruptured by wedge spallation at the end of the scratch track, which indicates this coating had poor bonding to the substrate. On the other hand, samples which were produced using the 5, 10, 15 and 20 minutes of modified single zincating process only exhibited cohesive failure as the progressive applied load increased, with no adhesive failure observed along the track. This means these coatings adhered well to the substrate. It is thought that a good coverage of zinc particles on the substrate enhances the uniform growth of the subsequent coating and increases the adhesion of the coating to the substrate (see also [10]).

4. CONCLUSION

SEM morphologies show that the size and density of zinc particles for single zincating with copper activation increased with increasing zincating duration. Coatings which were produced at a longer duration did

not show any delamination even at high progressive load. These coatings only experienced a cohesive failure mode, which means the coatings adhered well to the substrate. The sufficient coverage of zinc particles on the substrate has increased the adhesion between coating and the substrate.

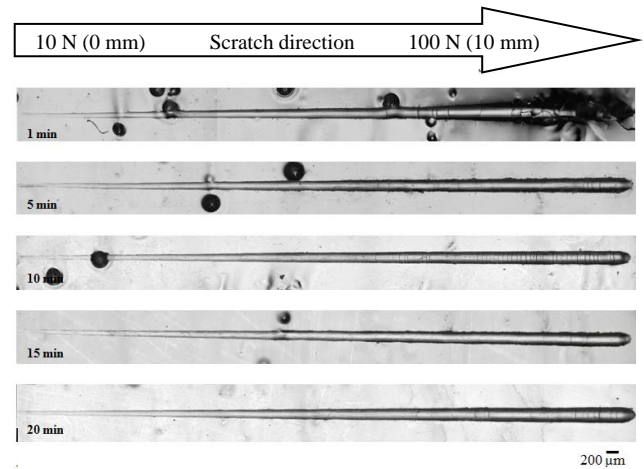


Figure 3 OM of the scratch tracks of nickel electrodeposited on AA7075 produced at various single zincating durations with copper activation.

ACKNOWLEDGEMENT

The authors would like to thank Ministry of Education Malaysia (KPT(BS)810526086238) for sponsoring this research. Also, thanks to Faculty of Engineering and the Environment, University of Southampton for the laboratory facilities and the chemical supplies.

REFE RENCES

- [1] Rajendran, R., Sha, W., & Elansezhian, R. (2010). Abrasive wear resistance of electroless Ni-P coated aluminium after post treatment. *Surface and Coatings Technology*, 205(3), 766-772.
- [2] Azumi, K., Yugiri, T., Kurihara, T., Seo, M., Habazaki, H., & Fujimoto, S. (2003). Direct plating of electroless Ni-P layers on sputter-deposited Al-Ni alloy films. *Journal of The Electrochemical Society*, 150(7), C461-C464.
- [3] Schwankl, M., Wedler, J., & Körner, C. (2016). Wrought Al-Cast Al compound casting based on zincate treatment for aluminum wrought alloy inserts. *Journal of Materials Processing Technology*, 238, 160-168.
- [4] Tang, J., & Azumi, K. (2011). Effect of copper pretreatment on the zincate process and subsequent electroplating of a protective copper/nickel deposit on the AZ91D magnesium alloy. *Electrochimica Acta*, 56(24), 8776-8782.
- [5] Sudagar, J., Venkateswarlu, K., & Lian, J. (2010). Dry sliding wear properties of a 7075-T6 aluminum alloy coated with Ni-P (h) in different pretreatment conditions. *Journal of Materials Engineering and Performance*, 19(6), 810-818.
- [6] Lee, J. H., Lee, I. G., Kang, T., Kim, N. S., & Oh, S. Y. (2005). The effects of bath composition on the morphologies of electroless nickel under-bump

- metallurgy on Al input/output pad. *Journal of Electronic Materials*, 34(1), 12-18.
- [7] Robertson, S. G., Ritchie, I. M., & Druskovich, D. M. (1995). A kinetic and electrochemical study of the zincate immersion process for aluminium. *Journal of applied electrochemistry*, 25(7), 659-666.
- [8] Azumi, K., Egoshi, S., Kawashima, S., & Koyama, Y. (2007). Effect of copper pretreatment on the double zincate process of aluminum alloy films. *Journal of The Electrochemical Society*, 154(4), D220-D226.
- [9] Egoshi, S., Azumi, K., Konno, H., Ebihara, K., & Taguchi, Y. (2012). Effects of minor elements in Al alloy on zincate pretreatment. *Applied Surface Science*, 261, 567-573.
- Jin, J. G., Lee, S. K., & Kim, Y. H. (2004). Adhesion improvement of electroless plated Ni layer by ultrasonic agitation during zincating process. *Thin Solid Films*, 466(1-2), 272-278.

Surface characterization of oxide films formed on aluminium alloy with the incorporation of graphite

Syazwani Mohamad, Shahira Liza Kamis*, Jun Ishimatsu

TriPreM *i-Kohza*, Mechanical Precision Engineering Department, Malaysia - Japan International Institute of Technology (MJIT), Universiti Teknologi Malaysia, Jalan Sultan Yahya Petra, 54100 Kuala Lumpur, Malaysia

*Corresponding e-mail: shahiraliza@utm.my

Keywords: Aluminum alloy; anodic composite film; surface porosity

ABSTRACT – Hard anodizing represents useful surface treatment on aluminium alloy which provide good microhardness and wear resistance. Graphite is a good reinforcement in the oxide film due to its good mechanical, low friction and self - lubricating behavior. Thus, the aim of this research is to investigate the growth mechanism of oxide film surface containing graphite. The surface morphology and 3D images were observed on scanning electron microscopy and 3D profiler respectively. The film structure was examined by Raman spectroscopy. The result showed the surface porosity was reduced when comparing to the oxide film without graphite. Raman spectra of D and G peak proved the existence of graphite on the oxide film surface can be observed in early 5 min of anodizing process.

1. INTRODUCTION

Aluminium (Al) alloy is one of the light weight and high strength materials which widely being used in aircraft, aviation industries and automotive parts such as power transmission gears, sprockets, drill pipes and engineering tools [1]. However, low hardness and poor wear resistance are the main obstacles to prolong the service life of Al alloys and further industrial applications as mentioned by Yang et al. [2]. Although surface modification like anodizing had been introduced to improve their surface properties, it is complicated to serve complex heat treatable Al alloy like 2XXX series that has high constituents of copper as alloying element which disturb the oxide layer formation during anodization process [3]. Some intermetallic precipitates (e.g. Al_2Cu , Al_2CuMg) in Al alloy 2XXX may cause difficulty in order to get a hard and compact oxide layer [4]. In addition, oxygen evolution induced porous structure of the oxide layer and lead to highly flaws on the surface. These issues have received considerable critical attentions from many researchers by improving the parameters of the anodizing process.

The incorporation of particles such as TiO_2 , ZrO_2 , Al_2O_3 , SiC and PTFE in the matrix of the oxide films had improved its hardness and tribological properties as stated by Kamis and Sofi [5]. Indeed, graphite may be a good candidate as reinforcement particle due to its good mechanical properties and low friction. However, the surface characterization of oxide film containing graphite is still less study. The aim of this research is to study the surface properties based on the incorporation of graphite particles in the oxide film produced by anodizing process.

2. METHODOLOGY

Anodization was performed on Al alloy A2017-T4 disk with diameter Ø25 mm and thickness 4 mm by using the laboratory anodizing system as shown in Figure 1 that consist of a direct current (DC) power supply and an electrolytic solution contains 20 wt. % diluted sulfuric acid with graphite. The graphite was added into the electrolyte. The anodizing process was experimented by using a constant current (2.0 A) and operating fluctuant voltage (± 15 V) of DC power supply. The cell consisted of a copper plate 30 mm x 60 mm at the cathode and the specimen as the anode. The temperature of electrolyte was kept at the room temperature. Firstly, the samples were anodized with 1.0 g/L of graphite contains at different times, being 5, 30 and 60 min respectively. After that, anodization process was continued by using different content of graphite; 0 g/L, and 1.0 g/L in order to clarify the improvement of mechanical and tribological characteristic of oxide films compared to the neat Al alloy.

The surface morphology will be characterized by using spectroscopy electron microscopy (SEM) JEOL JSM-6010PLUS/ LV. The 3D optical surface profiler ZeGage™ Ultra Precision Technology AMETEK (Zygo) was used to determine the 3D image profiling and to verify the size of micropores. Raman spectroscopy mainly be used to determine the structure of films and the existence of graphite in the oxide films.

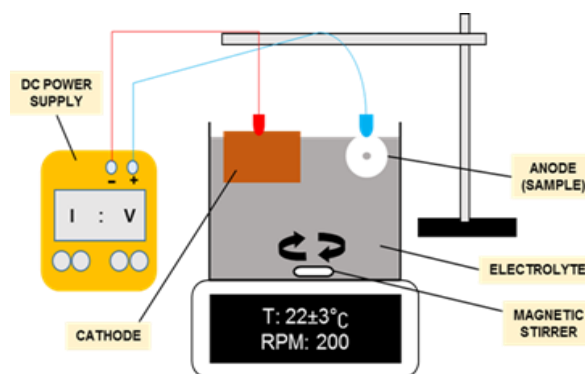


Figure 1 The schematic diagram of anodizing setup.

3. RESULTS AND DISCUSSION

Figure 2 shows the surface morphology of oxide films containing graphite at 5, 30, and 60 min. Anodize oxide film with graphite at 5 min, the surface morphology is seemed quite similar to the neat Al alloy which consist of a circle and granulate shapes of intermetallic precipitates where they can be clarified as the initial stage

of the growing oxide film. At 30 min, the obvious porosity started to form on the film and at 60 min, the films seem compact as longer time, but it still cannot determine the bumps or pores of films. In order to prove the assumption, the 3D image of oxide films at 5 min, 30 min and 60 min were studied as shown in Figure 2. It can be seen that the porosity started to develop at 30 min. The depth and width of porosity were found to increase as the longer anodizing duration as shown in Table 1. Thus, the time can affect surface defect of oxide film.

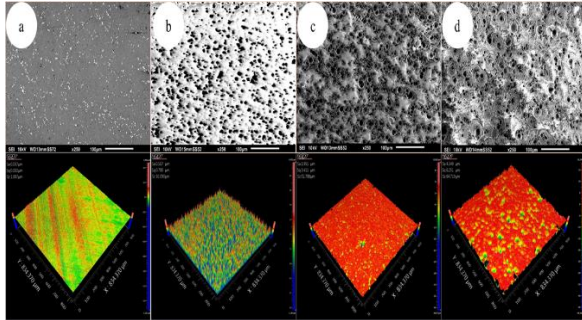


Figure 2 Surface morphology and 3D surface profile of neat Al alloy and oxide films with graphite at different anodizing time: (a) neat Al alloy (b) 5 min (c) 30 min (d) 60 min.

Table 1 The depth and width porosity measurement of oxide films containing graphite.

| | 5 min | 30 min | 60 min |
|---|-------|--------------------|---------------------|
| Depth (μm) | - | 28.7217 ± 6.02 | 38.227 ± 5.99 |
| Width (μm) | - | 33.6054 ± 3.75 | 63.5547 ± 14.13 |

However, when comparing the surface morphology and 3D surface profile of oxide films with and without graphite as shown in Figure 3, it proved that the addition of graphite had reduced the surface porosity. This could be due to the graphite embedded in the pores and reduce the porosity [5]. Peak of carbon around 1350 cm^{-1} (D-peak) and 1580 cm^{-1} (G-peak) can be clearly seen in Figure 4 which indicate that the graphite had incorporated into oxide films at the early 5 min.

4. CONCLUSION

Graphite can significantly improve the surface properties of oxide film. The growth of oxide film containing graphite seemed to enhance the surface porosity when increasing the anodizing duration. However, the surface porosity of oxide film containing graphite was reduced compared to the oxide film without graphite. This porosity reduction can significantly contribute as a good technology material for wide range mechanical applications.

ACKNOWLEDGEMENT

The author acknowledges the financial help provided by Universiti Teknologi Malaysia through Tier2 research grant No. Q. K130000.2643.15J17.

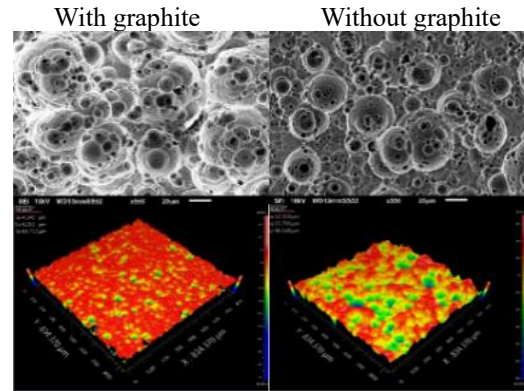


Figure 3 Surface morphology and 3D surface profile of oxide films with and without graphite at 60 min of anodizing time.

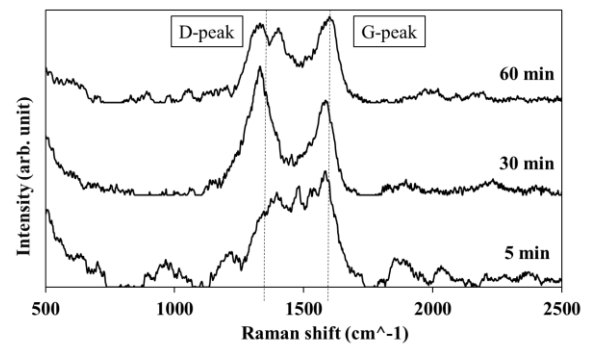


Figure 4 Raman spectra of oxide films with graphite at different anodizing time: (a) 5 min (b) 30 min (c) 60 min.

REFERENCES

- [1] Jung, J., Oak, J. J., Kim, Y. H., Cho, Y. J., & Park, Y. H. (2017). Wear behaviors of pure aluminum and extruded aluminum alloy (AA2024-T4) under variable vertical loads and linear speeds. *Metals and Materials International*, 23(6), 1097-1105.
- [2] Yang, F., Qin, Q., Shi, T., Chen, C., & Guo, Z. (2019). Surface strengthening aluminum alloy by in-situ TiC-TiB₂ composite coating. *Ceramics International*, 45(4), 4243-4252.
- [3] Zalnezhad, E., Sarhan, A. A., & Hamdi, M. (2013). Investigating the effects of hard anodizing parameters on surface hardness of hard anodized aerospace AL7075-T6 alloy using fuzzy logic approach for fretting fatigue application. *The International Journal of Advanced Manufacturing Technology*, 68(1-4), 453-464.
- [4] Zhao, X., Liu, W., Zuo, Y., & Yang, L. (2009). The cracking behaviors of anodic films on 1050 and 2024 aluminum alloys after heating up to 300°C. *Journal of Alloys and Compounds*, 479(1-2), 473-479.
- [5] Kamis, S. L., & Sofi, M. L. N. M. (2018). Fabrication of hard composite anodic films on aluminium alloy. *Proceedings of Mechanical Engineering Research Day 2018*, 2018, 228-229.

Optimization of waste cooking oil enhanced with hBN nanoparticles

Muhammad Ilman Hakimi Chua Abdullah^{1,2,*}, Aliatul Syafiqah Nabilah Mohamad¹, Abdul Munir Hidayat Syah Lubis^{1,2}, Adam Samsudin³, Mohd Afdhal Shamsudin^{1,2}, Mohd Fadzli Bin Abdollah^{2,4}

¹⁾Fakulti Teknologi Kejuruteraan Mekanikal dan Pembuatan, Universiti Teknikal Malaysia Melaka, Hang Tuah Jaya, 76100 Durian Tunggal, Melaka, Malaysia

²⁾Centre for Advanced Research on Energy, Universiti Teknikal Malaysia Melaka, Hang Tuah Jaya, 76100 Durian Tunggal, Melaka, Malaysia

³⁾Advance Manufacturing Center, Universiti Teknikal Malaysia Melaka, Hang Tuah Jaya, 76100 Durian Tunggal, Melaka, Malaysia

⁴⁾Fakulti Kejuruteraan Mekanikal, Universiti Teknikal Malaysia Melaka, Hang Tuah Jaya, 76100 Durian Tunggal, Melaka, Malaysia

*Corresponding e-mail: ilmanhakimi@utem.edu.my

Keywords: WCO; hBN; nanoparticles; friction, wear

ABSTRACT – The aims of this study is to determine the optimal design parameters in obtaining the lowest coefficient of friction (COF) and wear by hexagonal boron nitride (hBN) nanoparticles, dispersed in waste cooking oil. L9 orthogonal arrays was constructed using the Taguchi method to determine significant parameter contribution. Four-ball tester is used for conducting tribological testing according to ASTM standard D4172. By referring to analysis of S/N ratio, COF and wear scar was reduced significantly with addition hBN nanoparticles into the treated waste cooking oil. As conclusion, hBN nanoparticles promising to be next future additive for plant oil.

1. INTRODUCTION

Utilization of the plants and animals' oils had been practiced in industrial application for many years especially in lubricant fields due to economic impact and environmental concern. Plants oils-based lubricants shown an excellent in lubricity and may lead to major used in industries. This is because oil from plants has superior viscosity index and great anticorrosion properties which suitable towards metallic surface [1]. Besides, it also included with a property of non-flammability, non-polluting, non-toxic, and biodegradable to nature [2].

According to Panadre et al. [3] the use of the waste cooking oil is one of the afford to reduce the pollution occur. Vegetable-based oil is highly recommended utilized in industries due the potential of the oil in the lubricant is high. The significant advantages of vegetable oil to an environment such as ecological and possessed acceptable performance in a variety of utilization help researcher to study the potential of vegetable oil as a new lubricant. However, the vegetable/plant oil has its weakness which is they volatile for a long period of using for high temperature. Therefore, it needs an additive to overcome this problem. Most recommended additives nowadays are toward nanoparticles.

This study focuses on the capability of hBN as a new additive with suitable homogenized parameter on the tribological properties for optimized parameter on waste cooking oil.

2. EXPERIMENTAL SETUP

The samples composition was prepared according to Table. 1 and the Table. 2 for L9 orthogonal arrays for testing condition. The sample was homogenized shown in Figure 1.

Table 1 Sample parameters.

| Level | Parameters | | |
|-------|--------------|---------------------|------------|
| | hBN (vol. %) | Oleic acid (vol. %) | Time (min) |
| 1 | 0 | 0 | 20 |
| 2 | 0.25 | 0.1 | 30 |
| 3 | 0.5 | 0.3 | 40 |

Table 2 L9 Orthogonal arrays Taguchi method.

| Test | Parameters | | |
|------|--------------|---------------------|------------|
| | hBN (vol. %) | Oleic acid (vol. %) | Time (min) |
| 1 | 0 | 0 | 20 |
| 2 | 0.25 | 0.1 | 30 |
| 3 | 0.5 | 0.3 | 40 |
| 4 | 0.25 | 0.1 | 30 |
| 5 | 0.5 | 0.3 | 40 |
| 6 | 0 | 0 | 20 |
| 7 | 0.5 | 0.3 | 40 |
| 8 | 0 | 0 | 20 |
| 9 | 0.25 | 0.1 | 30 |

Tribological testing was performed to identify the coefficient of friction (COF) and wear rate accordance to ASTM D 4172 followed by scanning electron microscope (SEM).

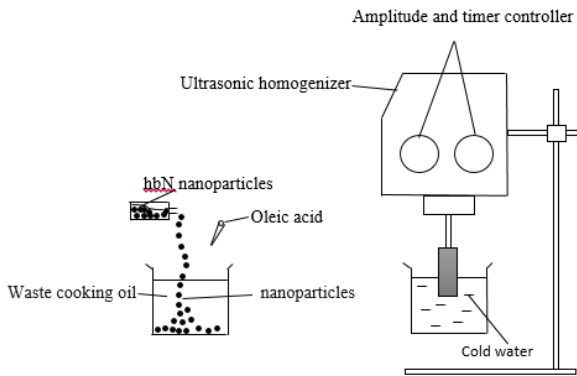


Figure 1 Homogenized process for sample preparation.

3. RESULTS AND DISCUSSION

According to the S/N ratios analysis shows by Figure 2, the optimal parameter obtained was 0.5 vol.% of hBN nanoparticles composition with 0.3 vol.% Oleic acid and 40 minutes of homogenized time. This optimized value reflex on sample 5 based on the L9 orthogonal arrays. Based on the result, all parameter shows the same significant contribution in obtaining the lowest friction and wear.

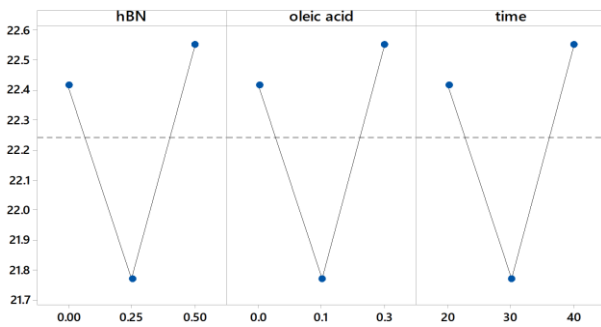


Figure 2 Main effects plot for S/N ratios.

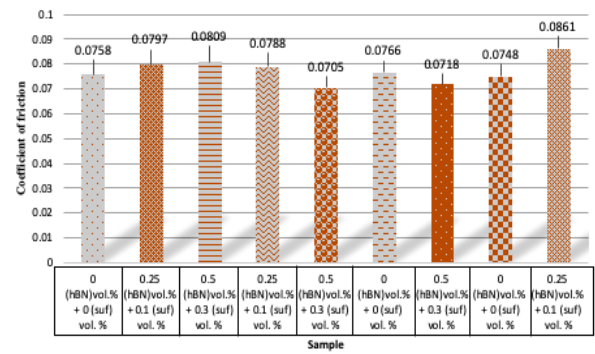
Figure 3(a) shows the CoF result obtained for all the tested sample which show the optimal result give the lowest CoF value, while Figure 3(b). shows the wear scar diameter for contributed sample as references. Higher composition of hBN resulting on lowest CoF and WSD which coherence with other work [4], which stated that hBN nanoparticles able to reduce the wear and friction of the contacting surface. The morphological contact surfaces show in Figure 4.

4. CONCLUSION

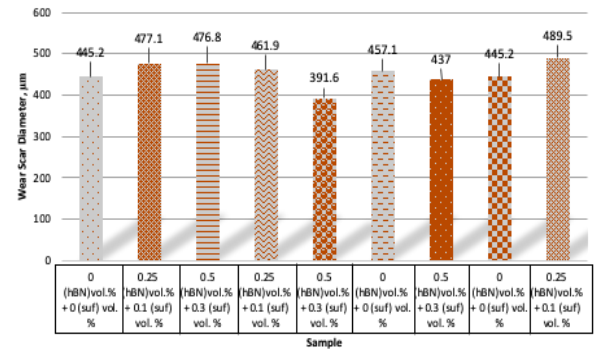
The optimal parameter for obtaining the lowest CoF and WSD is given by 0.5 vol.% of hBN nanoparticles composition with 0.3 vol.% Oleic acid and 40 minutes of homogenized time. Further investigation may help in term of developing stable WCO as new lubricant with help of hBN nanoparticles.

ACKNOWLEDGEMENT

The author would like to thank Universiti Teknikal Malaysia Melaka for funding this research under short Grant Scheme (PJP/2019/FTKEE(3A)/S01655).



(a)



(b)

Figure 3 (a) Average CoF value and (b) average WSD obtained for tested samples.

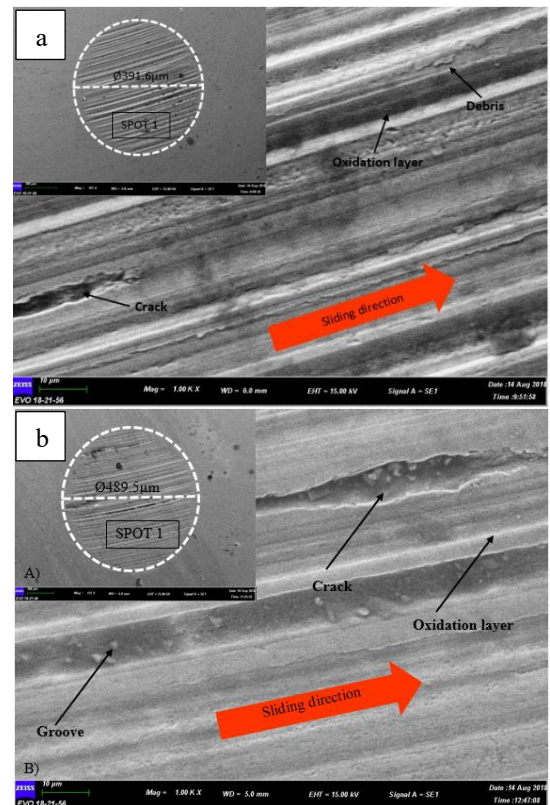


Figure 4 (a) Contact surface for sample optimized parameter (sample 5) and (b) worse condition (sample 9).

REFERENCES

- [1] Abdullah, M. I. H. C., Talip, J., Abdollah, M. F. B., & Jumaidin, R. (2018). Optimization of tribological performance for filtration waste cooking oil enhance by ZrO₂ and graphite nanoparticle. *Proceedings of Mechanical Engineering Research Day, 2018*, 111-112.
- [2] Kulkarni, M. G., & Dalai, A. K. (2006). Waste cooking oil an economical source for biodiesel: a review. *Industrial & Engineering Chemistry Research*, 45(9), 2901-2913.
- [3] Panadare, D. C. (2015). Applications of waste cooking oil other than biodiesel: a review. *Iranian Journal of Chemical Engineering*, 12(3), 55-76.
- [4] Abdullah, M. I. H., Abdollah, M. F. B., Amiruddin, H., Tamaldin, N., Nuri, N. R. M., Masjuki, H., & Rafeq, S. A. (2014). Improving engine oil properties by dispersion of hBN/Al₂O₃ Nnanoparticles. *Applied Mechanics and Materials*, 607, 70-73.

Tribological influence of hBN and MoS₂ nanoparticles as additive in modified jatropha based oil nanofluids

Norfazillah Talib^{1,*}, Shahirah Azua A Khalid¹, Lee Woon Kiow¹, Haslina Abdullah¹, Nor Athirah Jamaluddin¹, Aslinda Saleh²

¹) Faculty of Mechanical and Manufacturing Engineering, Universiti Tun Hussein Onn Malaysia, 86400 Batu Pahat, Johor, Malaysia

²) Faculty of Engineering Technology, Universiti Tun Hussein Onn Malaysia, Pagoh Higher Education Hub, 84600 Pagoh, Muar, Johor, Malaysia

*Corresponding e-mail: fazillah@uthm.edu.my

Keywords: Tribology; nanoparticle; nanofluid

ABSTRACT – Nanofluid has attracted great interest to be studied in recent years due to its potential as machining lubricant. The aim of this study is to investigate the influence of nanofluids from modified jatropha based oil (MJO) in term of tribological characteristic. MJO was mixed with hBN and MoS₂ nanoparticles at 0.05wt.% concentration. The nanofluid samples were compared with synthetic ester through four ball test. The results found that the usage of nanofluids (MJO+hBN and MJO+MoS₂) showed excellent tribological characteristic compared to SE and have the potential to substitute SE as the sustainable lubricant.

1. INTRODUCTION

Tribological characteristic is the most important consideration in selecting a suitable lubricant. It relates to the lubricant performance in terms of lubricity, friction and wear which associated with the formation of lubrication film or tribofilm on the sliding surfaces. The addition of nanoparticles additives in the based oil known as nanofluid promised a significant effect on the tribological characteristic. Padmini et al. [1] identified that the usage of nanofluid was found to form consistent lubrication film separating the contact surfaces thus imparts a better surface quality of the workpiece.

This finding similar to the study by Kong et al. [2] which indicates that the usage of nanoparticles ultimately lowers the friction coefficient. They stated that nanoparticles provided a rolling mechanism theory and form a sliding system thus reducing the friction and wear. Moreover, Kim et al. [3] found that the usage of nanoparticles in the vegetable based fluid was advantageous to reduce friction and increase the thermal conductivity of the nanofluid. The results found that the usage of nanofluids during the micro-end-milling process significantly reduced the forces.

In this study, the modified jatropha oils with the addition of 0.05wt.% of hBN and 0.05wt.% of MoS₂ were compared with synthetic ester through four-ball test. The testing results were discussed in terms of coefficient of friction, wear scar diameter and the worn surface analysis.

2. METHODOLOGY

2.1 Lubricant Preparation

Modified jatropha based oil (MJO) was formulated through the transesterification process of jatropha methyl

ester and trimethylolpropane at the molar ratio of 3.5:1 in the presence of 1% (wt./wt.) sodium methoxide. Previously, MJO has been proved to offer better lubrication properties [4]. Hexagonal boron nitride (hBN) and molybdenum disulfide (MoS₂) with a diameter of 100nm were used as the nanoparticles. Both particles were used as the additives and blended with MJO at the weight concentration of 0.05wt.% to obtain nanofluid. The nanofluids were compared with the synthetic ester (Unicut Jinen MQL) as the reference oil as shown in Table 1.

Table 1 Oil samples.

| Samples | Description |
|----------------------|------------------------------------|
| MJO+hBN | MJO with 0.05wt.% hBN |
| MJO+MoS ₂ | MJO with 0.05wt.% MoS ₂ |
| SE | Synthetic ester |

2.2 Tribology Test

Tribological characteristic was evaluated through four ball test using tribotester according to ASTM D4712. This testing used a new set of four steel balls (AISI52100) with a diameter of 12.7 mm. Prior to this, three stationary balls were clamped together as shown in Figure 1. 10 ml nanofluid sample was poured into the ball pot. The rotating ball was locked inside the container and stripped into the spindle. The ball pot assembly was mounted in the tribotester machine. The normal load of 392 ± 2N was pressed slowly at the stationary balls. The operating temperature was regulated at 75± 2°C. The rotating ball was rotated at the constant speed of 1200 rpm for 60 minutes of operation time. The coefficient of friction (COF) was determined by the Winducom 2010 software. The wear scar diameter of the stationary balls was measured through an optical microscope. The morphology of the worn surfaces was analyzed via a scanning electron microscope (SEM).

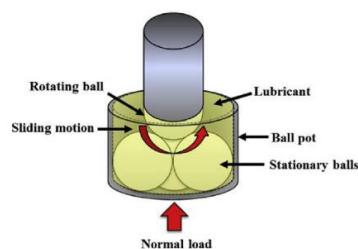


Figure 1 Four ball test set up [5].

3. RESULTS AND DISCUSSION

Figure 2 shows that SE recorded the highest COF of 0.098 and WSD of 0.94 μm compared to nanofluid samples. MJO+hBN nanofluids exhibited the smallest COF of 0.048 and WSD of 0.523 μm . Meanwhile, the COF and WSD values of MJO+MoS₂ nanofluid was recorded at 0.05 and 0.544 μm , respectively. The COF and WSD values of MJO+hBN and MJO+MoS₂ were improved by 49 to 51 % and 42 to 44 % compared to SE. The usage of both nanofluids sample demonstrated the lowest value of COF and WSD. This phenomenon occurs due to the presence of long and branched carbon chains in MJO that provided excellent lubrication layer [5]. In addition, the presence of a minimum concentration of hBN and MoS₂ nanoparticles (0.05wt.%) in MJO tended to form better protective films and cause a rolling effect at the contact surfaces [6]. The addition of nanoparticles in based oil can withstand compressive stress concentration subsequently reduced the friction and wear. Further, the addition of hBN nanoparticles in MJO provided better tribological property compared to the addition of MoS₂ in MJO. It was due to the crystalline structure of hBN nanoparticles that contributed to the excellent lubricating properties.

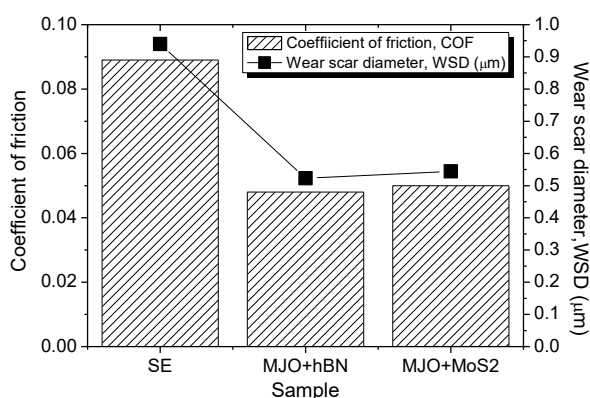


Figure 2 Results of four ball test

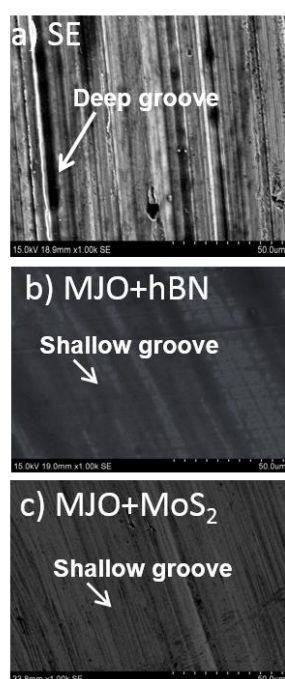


Figure 3 Morphology of the worn surfaces.

Figure 3 illustrated the surface morphology of the worn surfaces of all samples. It can be observed that the high COF of SE was proven by the formation of parallel deep groove on the worn surface as shown in Figure 3(a). This evidence proved that the lubrication film form by SE was not able to support the applied load during the operation time. Furthermore, a few parallel shallow grooves found on the worn surface of MJO+hBN and MJO+MoS₂ as shown in Figures 3(b) and 3(c). The results revealed that both nanofluids form an adequate lubrication thin layer that able to withstand the friction at the contact surfaces resulting low COF.

4. CONCLUSION

The results of the four-ball test showed that the presence of minimum concentration (0.05wt.%) of nanoparticles additive in modified jatropha oils nanofluid successfully enhanced the tribological properties by reducing the COF and WSD. Moreover, the addition of hBN nanoparticles as the additive provided better lubrication film compared to MoS₂ nanoparticles. It can be concluded that, both nanofluids have a potential to substitute SE as the sustainable lubricant.

ACKNOWLEDGEMENT

This work was supported by Universiti Tun Hussein Onn Malaysia and Ministry of Education Malaysia under the TIER 1 research grant (H176) and FRGS (K077).

REFERENCES

- [1] Alves, S. M., Schroeter, R. B., Bossardi, J. C. D. S., & Andrade, C. L. F. De. (2011). Influence of EP additive on tool wear in drilling of compacted graphite iron. *Journal of the Brazilian Society of Mechanical Sciences and Engineering*, 33(2), 197–202.
- [2] Dai, W., Kheireddin, B., Gao, H., & Liang, H. (2016). Roles of nanoparticles in oil lubrication. *Tribology International*, 102, 88–98.
- [3] Kim, J. S., Kim, J. W., & Lee, S. W. (2017). Experimental characterization on micro-end milling of titanium alloy using nanofluid minimum quantity lubrication with chilly gas. *International Journal of Advanced Manufacturing Technology*, 91(5–8), 2741–2749.
- [4] Kong, L., Sun, J., & Bao, Y. (2017). Preparation, characterization and tribological mechanism of nanofluids. *Royal Society of Chemistry*, 7(21), 12599–12609.
- [5] Talib, N., Nasir, R. M., & Rahim, E. A. (2017). Tribological behaviour of modified jatropha oil by mixing hexagonal boron nitride nanoparticles as a bio-based lubricant for machining processes. *Journal of Cleaner Production*, 147, 360–378.
- [6] Talib, N., & Rahim, E. A. (2018). Experimental evaluation of physicochemical properties and tapping torque of hexagonal boron nitride in modified jatropha oils-based as sustainable metalworking fluids. *Journal of Cleaner Production*, 171, 743–755.

Tribological properties characterization of green polyol

Abdul Munir Hidayat Syah Lubis^{1,2,*}, Adam Samsudin³, Jeefferie Abd Razak³,
Muhammad Ilman Hakimi Chua Abdullah^{1,2}, Amir Abdullah Muhamad Damanhuri^{1,2}, Khairul Amri Tofrowaih^{1,2},
Mohd Fariduddin Mukhtar¹

¹⁾ Fakulti Teknologi Kejuruteraan Mekanikal dan Pembuatan, Universiti Teknikal Malaysia Melaka,
Hang Tuah Jaya, 76100 Durian Tunggal, Melaka, Malaysia

²⁾ Centre for Advanced Research on Energy, Universiti Teknikal Malaysia Melaka,
Hang Tuah Jaya, 76100 Durian Tunggal, Melaka, Malaysia

³⁾ Advance Manufacturing Center, Universiti Teknikal Malaysia Melaka,
Hang Tuah Jaya, 76100 Durian Tunggal, Melaka, Malaysia

*Corresponding e-mail: munir@utem.edu.my

Keywords: Polyol; friction; wear

ABSTRACT – Awareness of mineral oil resources depletion has been increasing in the past decade which drive the utilization of bio-based lubricant. In this research, tribological properties of palm oil-based polyol was investigated. The viscosity, viscosity index, flash point, friction coefficient and wear preventive properties were observed by following corresponding ASTM standard testing. Palm oil-based polyol was found to possesses good friction and wear preventive properties. It also possessed higher viscosity, but lower viscosity index compared to palm oil. The polyol sample show higher coefficient of friction compared to palm oil and better wear preventive properties compared to palm oil.

1. INTRODUCTION

Bio-based lubricant has been acknowledged as alternative to petroleum-based lubricant. The use of vegetable oils as lubricant become popular again due to their good lubricating properties, from renewable sources, and more environmentally friendly. This kind of oil already used as lubricant long before the exploration of petroleum product in the 18th century. However, their application is still limited because of their oxidation properties, low and high temperature resistant, and storability. However, several researchers found that this disadvantages can be overcome by performing structural modification of the fatty acid contained in the vegetable oil [1].

Polyol is a type of organic compound containing two or more hydroxyl groups (OH groups) per molecule. Polyols from renewable are typically of trifunctional glycerol and hexafunctional sorbitol [2]. Polyol ester has been used as lubricant due to its excellent thermal and oxidation stability, lubricating properties and excellent viscosity characteristics at low temperatures [3]. Polyols can be synthesized through transesterification of vegetable oils with other polyols or alcohols, producing fatty acid polyol mono- and di-esters [4], [5]. The objective of this work is to investigate tribological properties of palm oil-based polyol as lubricant source.

2. METHODOLOGY

Palm oil-based polyols obtained from local polyol manufacturer was used as lubricant sample without any further treatment and palm oil was used as properties

comparison. Fourier Transformed Infra-Red (FTIR) analysis was conducted to analyse functional group of the polyol by using a JASCO-6100 FTIR analyser at scanning range of 500 cm⁻¹ – 4000 cm⁻¹. Kinematic viscosity of the sample was measured by using Kitiwake viscometer at temperature of 40°C and 100°C. Viscosity Index (VI) of the polyols sample was calculated based on ASTM D-2270 method. Flash point of the sample determined by closed cup method following ASTM D-93 standard. Friction and wear prevention properties of the sample was observed by Four ball methods according to ASTM D-4172. Scanning electron microscope (SEM) was employed to observed wear morphology of the solid sample lubricated with the polyol.

3. RESULTS AND DISCUSSION

FTIR spectra of the polyol sample is shown in Figure 1. Peaks at 3458 cm⁻¹ is shows absorption bands of the OH group and peak at 1740 cm⁻¹ is related to C-O stretching bond. Peaks in 1094 – 1240 cm⁻¹ region are belonging to C-O group stretching related to ester, ether and hydroxyl groups. Peaks at 2848 and 2920 cm⁻¹ are attributed to stretching of CH₃ groups and peaks at are attributed to bending of CH₂ groups [6]. Peak at 722 cm⁻¹ is correspond to the (CH₂)_n sequence of the aliphatic chains of the fatty acids [7].

Table 1. Viscosity and flash point of polyol sample.

| Properties | Viscosity @40°C | Viscosity @100°C | VI | Flash point |
|------------|--------------------|---------------------|-------|----------------|
| Polyol | 975.1 cS | 47.23 cS | 91.2 | 180°C |
| Palm Oil | 36.95 cS | 9.12 cS | 166.3 | 224°C |

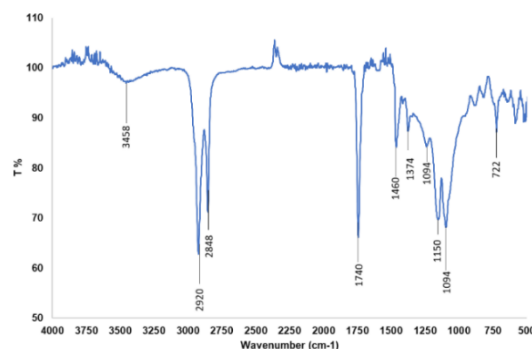


Figure 1 FTIR spectra of polyol sample.

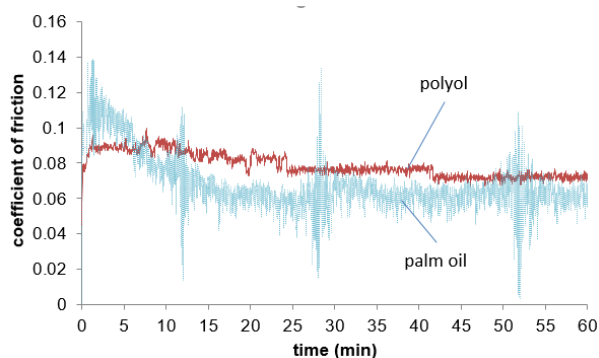


Figure 2 Friction graph of steel lubricated with polyol and palm oil.

Table 1 show the viscosity, viscosity index, and flash point of the polyol and palm oil. The polyol is thicker fluid with viscosity of 975,1 cS at 40°C and 47, 23 cS at 100°. However, the viscosity index of the polyol sample is 91.2, lower to the palm oil. The thicker viscosity is considered related to the molecular structure of the polyol sample. Flash point of the polyol sample also found lower than the palm oil sample.

Friction of the samples is shown in Figure 2. It is observed that the steel lubricated with the polyol sample exhibit initial friction coefficient of 0.085 then reduced to 0.071 with extension of sliding time. The lubricated friction of polyol was found higher than the palm oil (steady coefficient of friction = 0.064). Higher coefficient of friction of polyol compared to palm oil obtained is considered related to polyol's high viscosity causing more resistance during the sliding.

Figure 3 shows the SEM micrograph of wear scar observed on the steel ball sample. Wear scar diameter (WSD) of average 624 μm was obtained from sample lubricated with polyol and WSD of 660 μm was obtained from sample lubricated with palm oil. This result indicates that the palm oil-based polyol sample still possesses good friction and wear preventive properties like most vegetable oil. The morphology of the wear surface shows significant wear track at the center of wear circle (Figure 3a). Further magnification on the wear track indicating mild adhesive wear mechanism has been operated during the sliding (Figure 3b).

4. CONCLUSION

The palm oil-based polyol found to possesses good friction and wear preventive properties. It is also possessed higher viscosity, but lower viscosity index compared to palm oil. The polyol sample show higher coefficient of friction compared to palm oil which related to its high viscosity that cause resistance during sliding. Wear preventive properties of the polyol show a better result compared to palm oil.

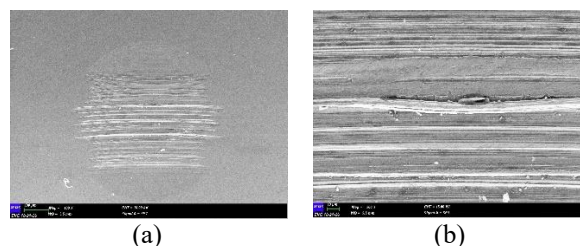


Figure 3 SEM Micrograph of steel ball worn surface, (a) 100X magnification, (b) 500X magnification.

ACKNOWLEDGEMENT

The authors would like to thank University Teknikal Malaysia Melaka for supporting this research under PJP grant no PJP/2019/FTKEE(3A)/S01655.

REFERENCES

- [1] Sharma, B. K., & Erhan, S. Z. (2013). 23 Modified Vegetable Oils for Environmentally Friendly Lubricant Applications. *Synthetics, Mineral Oils, and Bio-based Lubricants: Chemistry and Technology*, 385-411.
- [2] Rudnick, L. R. (2005). *Synthetics, mineral oils, and bio-based lubricants: chemistry and technology*. CRC press.
- [3] Mang, T., Dresel, W., & Wiley, J. (Eds.). (2007). *Lubricants and lubrication* (Vol. 2, pp. 185-190). Weinheim, Germany: Wiley-Vch.
- [4] Yunus, R., Fakhru'l-Razi, A., Ooi, T. L., Omar, R., & Idris, A. (2005). Synthesis of palm oil based trimethylolpropane esters with improved pour points. *Industrial & Engineering Chemistry Research*, 44(22), 8178-8183.
- [5] Hayes, D. G., & Dumont, M. J. (2016). Polymeric products derived from industrial oils for paints, coatings, and other applications. In *Industrial Oil Crops* (pp. 43-73). AOCS Press.
- [6] Radojčić, D., Ionescu, M., & Petrović, Z. S. (2013). Novel potentially biodegradable polyurethanes from bio-based polyols. *Contemporary Materials*, 1(4), 9-21.
- [7] Mizera, K., & Ryszkowska, J. (2016). Polyurethane elastomers from polyols based on soybean oil with a different molar ratio. *Polymer Degradation and Stability*, 132, 21-31.

Superhydrophilicity of laser surface textured TiO₂ coating for self-cleaning surfaces

Yusliza Yusuf^{1,2,*}, Mariyam Jameelah Ghazali¹, Mohd Fadzli Bin Abdollah³, Yuichi Otsuka⁴, Susumu Nakamura⁵

¹) Centre for Materials Engineering and Smart Manufacturing, Faculty of Engineering and Built Environment, Universiti Kebangsaan Malaysia, 43600 UKM Bangi, Selangor, Malaysia.

²) Fakulti Teknologi Kejuruteraan Mekanikal dan Pembuatan, Universiti Teknikal Malaysia Melaka, Hang Tuah Jaya, 76100 Durian Tunggal, Melaka, Malaysia.

³) Fakulti Kejuruteraan Mekanikal, Universiti Teknikal Malaysia Melaka, Hang Tuah Jaya, 76100 Durian Tunggal, Melaka, Malaysia

⁴) Department of System Safety, Nagaoka University of Technology, 1603-1 Kamitomioka Nagaoka, Niigata 940-2188, Japan

⁵) Department of Electrical and Electronic Systems Engineering, National Institute of Technology, Nagaoka College, 888 Nishikataai, Nagaoka, Niigata 940-8523, Japan

*Corresponding e-mail: yusliza@utem.edu.my

Keywords: Laser surface texturing; TiO₂; self cleaning

ABSTRACT – In this study, the effect of laser surface texturing on TiO₂ coating surface to create a self-cleaning surface was studied. The TiO₂ coating deposition was carried out on API steel substrate by using plasma spraying prior to laser texturing. Picosecond laser system was used to create a micro-dimpled texture on the TiO₂ surface. Laser texturing process changed the TiO₂ coating wettability properties from hydrophilic to superhydrophilic. The superhydrophilic properties showed that laser texturing is a facile method for developing self-cleaning TiO₂ surfaces, which are applicable for various industrial applications.

1. INTRODUCTION

Superhydrophobic surface (contact angle >150°) and superhydrophilic surfaces (contact angle~ 0°) have been broadly explored by researchers because of their significance for applications in modern times. The self-cleaning superhydrophilic surface spreads water droplets to form a film throughout itself, thereby, allowing light waves to pass through. Following this discovery, a rigorous study is in progress worldwide to analyse the mechanism and to develop superhydrophilic coatings.

Examples of TiO₂-derived materials have been discovered to understand the fundamental principles of self-cleaning with hydrophilic and hydrophobic surfaces. The hydrophilic character of TiO₂ was first reported by Wang et al. [1] in 1997. Wang et al. reported that TiO₂ film is irradiated with light, and the contact angle being reduced to 0° results in spreading of water droplets on the surface. The hydrophilic TiO₂ surface has been exploited commercially to develop anti-fogging and self-cleaning surface for various applications, such as fabrics, paints, glass and tiles (Table 1). Therefore, this study evaluated the effect of laser surface texturing on the properties of TiO₂-coated surfaces. Laser surface texturing involves creating different patterns on substrates and has been proven effective in improving surface features [6]. Immediately after laser texturing, the surface becomes either

hydrophilic or hydrophobic [6]. In this work, dimple structures were fabricated on TiO₂ coating through the use of a picosecond laser. The effect of dimples on the TiO₂ coating on the wettability properties was investigated.

Table 1 Uses of self cleaning materials.

| Substrate | Application | Ref |
|-----------------------|---|-----|
| Tiles | Kitchen, building roof and walls | [2] |
| Glass | Mirrors for vehicles and indoor uses, windows, tunnel, road light | [3] |
| Textiles | Hospitals garments, medical devices, protective clothing | [4] |
| Plastic/polycarbonate | Automotive industry and buildings | [5] |

2. METHODOLOGY

2.1 Preparation of TiO₂ Coating

Commercial titanium dioxide, TiO₂ (Metco 102 Oerlikon Metco ≥ 99.0 wt. %), with a nominal particle size distribution of 11-45 µm was used as raw materials. The coatings were deposited onto carbon steel API 5L grade B 30 cm (length) × 5 cm (width) × 7 mm (thickness) by using an atmospheric plasma spray system with SG-100 torch (Praxair, USA) mounted on ABB IRB Industrial robot. Prior the deposition, the substrate were grit-blasted and ultrasonically cleaned in ethanol and deionized water.

2.2 Laser Surface Texture Preparation

Areas with dimensions of 8 mm × 8 mm on the plasma sprayed TiO₂ coating were subjected to laser surface texturing. A laser manufacturing system (Q-switched Nd:YAG picosecond laser) was used to create a micro-dimpled texture on the TiO₂ surface. The dimple diameter, dimple depth and area density at 20µm, 7µm and 0.2% respectively. The morphologies of the textured surface were observed by using scanning electron microscope (SEM). The area density, AD is calculated from Eq.1 [7].

$$AD = \frac{\pi r^2}{16l^2} \quad (1)$$

2.3 Wettability Test

Surface wettability of the samples was evaluated by measuring the static contact angle (CA) with a CA analyser (DMe-201 Kyowa) using the 1 μ l sessile drop technique. All measurements were performed when the water droplets reached stability on the surface.

3. RESULTS AND DISCUSSION

3.1 Surface Morphology Using SEM

SEM images (Figure 1) revealed that the plasma-sprayed TiO₂ coating contained partially melted and unmelted particles that adhered to fully melted splats. The laser impact sites surrounding the dimples underwent material transformation. Ejected matter associated with the coating material can be observed around the dimples.

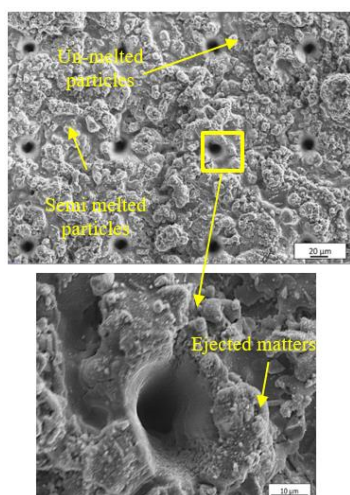


Figure 1 Surface SEM images of laser textured TiO₂ coating.

3.2 Surface Wettability

Surface wettability of the prepared laser-textured TiO₂ coating was evaluated by measuring the static CA. An increase of CA indicated decreased wettability. Comparison of the CA of the laser-textured TiO₂ coating with non-textured surface is shown in Figure 2. Each data point presents an average of over three dimensions.

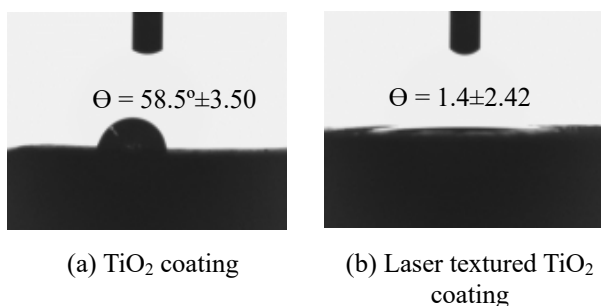


Figure 2 Contact angle of TiO₂ coating.

The initial TiO₂ coating (non texture) was hydrophilic with a CA of 58.5°. After the laser ablation, all the samples exhibited superhydrophilic behaviour with low CA of less than 4°. This may be attributed to the modifications of chemical composition (hydroxyl

group) and surface morphology during laser texturing [6]. The superhydrophilic properties obtained in this study showed a facile method to develop a self-cleaning TiO₂ surface. The surface water drops spread over the surface of laser-textured TiO₂ and form a water film. During spreading, the contamination on the surface was washed away [8].

4. CONCLUSION

Experimental results indicated that the wettability properties of TiO₂ coating changed from hydrophilic to superhydrophilic after laser texturing. This study may provide a potential facile method to construct textured surfaces that undergo changes with wetting behaviour, thereby extending the industrial applications especially for pipeline usage.

ACKNOWLEDGEMENT

The authors thank Universiti Kebangsaan Malaysia and Nagaoka University of Technology Japan for their support and cooperation during the conduction of the experiments. The authors acknowledge Universiti Teknikal Malaysia Melaka for financially supporting the authors' Ph.D.

REFERENCES

- [1] Wang, R., Hashimoto, K., Fujishima, A., Chikuni, M., Kojima, E., Kitamura, A., ... & Watanabe, T. (1997). Light-induced amphiphilic surfaces. *Nature*, 388(6641), 431.
- [2] Xie, T. H., & Lin, J. (2007). Origin of photocatalytic deactivation of TiO₂ film coated on ceramic substrate. *The Journal of Physical Chemistry C*, 111(27), 9968-9974.
- [3] Takata, Y., Hidaka, S., Cao, J. M., Nakamura, T., Yamamoto, H., Masuda, M., & Ito, T. (2005). Effect of surface wettability on boiling and evaporation. *Energy*, 30(2-4), 209-220.
- [4] Liu, K., Cao, M., Fujishima, A., & Jiang, L. (2014). Bio-inspired titanium dioxide materials with special wettability and their applications. *Chemical reviews*, 114(19), 10044-10094.
- [5] Yaghoubi, H., Taghavinia, N., & Alamdari, E. K. (2010). Self cleaning TiO₂ coating on polycarbonate: surface treatment, photocatalytic and nanomechanical properties. *Surface and coatings technology*, 204(9-10), 1562-1568.
- [6] Yan, H., Rashid, M. R. B. A., Khew, S. Y., Li, F., & Hong, M. (2018). Wettability transition of laser textured brass surfaces inside different mediums. *Applied Surface Science*, 427, 369-375.
- [7] Mohmad, M., Abdollah, M. F. B., Tamaldin, N., & Amiruddin, H. (2018). Frictional characteristics of laser surface textured activated carbon composite derived from palm kernel. *The International Journal of Advanced Manufacturing Technology*, 95(5-8), 2943-2949.
- [8] Banerjee, S., Dionysiou, D. D., & Pillai, S. C. (2015). Self-cleaning applications of TiO₂ by photo-induced hydrophilicity and photocatalysis. *Applied Catalysis B: Environmental*, 176, 396-428.

Various quarry dust content influences the tribological properties of Ni-P composite coating

Muhamad Ammar Farhan Maula Mohd Azam¹, Intan Sharhida Othman^{1,*}, Mohd Shahir Kasim¹,
Jariah Muhamad Juoi¹, Mohd Rody Bin Mohamad Zin²

¹Fakulti Kejuruteraan Pembuatan, Universiti Teknikal Malaysia Melaka,
Hang Tuah Jaya, 76100 Durian Tunggal, Melaka, Malaysia

²Fakulti Kejuruteraan Mekanikal, Universiti Teknikal Malaysia Melaka,
Hang Tuah Jaya, 76100 Durian Tunggal, Melaka, Malaysia

*Corresponding e-mail: intan_sharhida@utem.edu.my

Keywords: Electrodeposition; quarry dust; wear

ABSTRACT – The advance and overview of new coated cutting tool carry out several studies with the purpose to optimize the coatings content. Nickel-phosphorus-quarry dust (Ni-P-QD) composite coatings using various quarry dust (QD) content were deposited on tungsten carbide substrate by using an electrodeposition technique. The electrodeposition process was carried out for 1 hour at 40°C under the current density of 3 A/dm² in a modified nickel Watt's bath containing 20, 60, and 100 g/l of quarry dust particles. The effects of quarry dust content on the hardness and wear properties of electrodeposited Ni-P-QD composite coatings on WC substrate were investigated before and after heat treatment. As the quarry dust content increases, the hardness and wear resistance also improved, due to the presence of high silica and alumina content in the quarry dust particles.

1. INTRODUCTION

Numerous cutting tools have been developed continuously since the first cutting tool material suitable for use in carbon steel, metal cutting, was industrialized a century ago [1]. As in the case of the machining, Ayed et al. [2] conducted machining of Ti17 with uncoated tungsten carbide tools under different cutting environments. Notch wear, plastic deformation, adhesion and abrasion wear were found to be the main wear mechanisms during machining. Coatings are applied to improve surface properties of the substrate, such as mechanical properties, adhesion, corrosion, wettability, wear resistance, lubrication, and scratch resistance [3-5]. The properties of Ni-P can be improved by co-deposition with hard particles (e.g. SiC, WC, Al₂O₃) and dry lubricant (e.g. MoS₂) [6]. In this study, quarry dust particles were added to the Ni-P solution. Quarry dust is one of the by- product from quarrying activities which lead to waste management proposal. The quarry dust can be employed as inexpensive strengthening particles which can increase wear resistance and enhanced microhardness due to presence of high SiO₂ and Al₂O₃ in the particles [7]. Thus, Ni-P-QD composite coatings were introduced by using electrodeposition technique. The present work is aimed to investigate the effect of various quarry dust content and heat treatment process on the properties of Ni-P-QD composite coatings electrodeposited on tungsten carbide substrate.

2. METHODOLOGY

The tungsten carbide substrate with dimension of 40 mm x 30 mm x 3 mm were grind using silicon carbide paper from 240 to 1200 grit paper and polished with diamond paste 0.3µm. Then, substrate was cleaned with ethanol and acetone for 20s to remove the oily surface of the substrate. The substrate was then attached to a glass cell fitted with a water jacket, through which water from a thermostat bath was circulated. A power supply was employed for nickel electrodeposition using a typical two-electrode system consisting of anode electrode nickel plate (99.99%) and cathode electrode of tungsten carbide plate. The chemical composition and operating condition for electrodeposition of Ni-P-QD composite coating were summarized in Table 1.

Table 1: Composition of modified nickel Watt's bath and electrodeposition operating condition.

| Modified Watt's bath solution | |
|---|---------------------|
| Chemical compound | Content (g/l) |
| NiSO ₄ .6H ₂ O | 200 |
| NiCl ₂ .6H ₂ O | 20 |
| C ₆ H ₅ Na ₃ O ₇ .2H ₂ O | 30 |
| NaH ₂ PO ₂ | 10 |
| Quarry Dust | 20,60,100 |
| Condition Parameter Electrodeposition | |
| Time | 1 hour |
| Temperature | 40°C |
| Current | 3 A/dm ² |
| Speed | 300 rpm |

3. RESULTS AND DISCUSSION

3.1 Characterization of Quarry Dust

The elemental composition for quarry dust particles is found by XRF technique and shown in Table 2.

Table 2 Composition of quarry dust particles.

| Element | SiO ₂ | Al ₂ O ₃ | CaO | Fe ₂ O ₃ | MgO | Na ₂ O | K ₂ O | SO ₃ | TiO ₂ | P ₂ O ₅ |
|---------------------|------------------|--------------------------------|-----|--------------------------------|-----|-------------------|------------------|-----------------|------------------|-------------------------------|
| Concentration (Wt%) | 72.6 | 15.1 | 1.1 | 1.9 | 0.8 | 3.0 | 4.9 | 0.2 | 0.3 | 0.1 |

3.2 Effect of Various Quarry Dust Content on The Wear Scar of Composite Coatings

From SEM image of wear scar of Ni-P-QD 20,60 and 100 g/l with (Figure 2 (b,d,f)) and without heat treatment (Figure 2 (a,c,e)) shows that's worn area of

the samples. The scar presents a ploughing wear. The wear scar improves after the heat treatment at 200°C within increasing of the QD content due to the existing of Si and Al₂O₃ in the composite coatings.

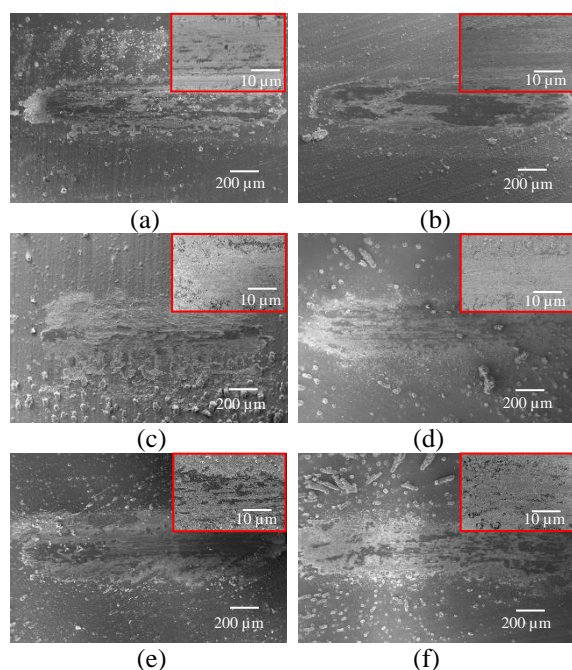


Figure 2 (a) 20 g/l QD (b) 20 g/l QD heat treatment (c) 60 g/l QD (d) 60 g/l QD heat treatment (e) 100 g/l QD (f) 100 g/l QD heat treatment.

Overall, the microhardness value of the Ni-P-QD coating shows an improvement by increasing the quarry dust content and applying a heat treatment process to the coated substrate (Figure 3). Due to the heat treatment process its can be shown that at Ni-P-QD 60 g/l the microhardness increases from 876.6 HV to 972.3 HV. This finding is consistent with the XRD analysis in Figure 4 which reported that the present peak of the Ni₃P phase at 31.5° and 48.8° is present and produce intermediate layer between coating and substrate will enhance the microhardness properties of the coatings. There are several reports concerning the phase transformation within the Ni-P plating in which various temperature and heating rates were applied. Keong et al. [8] revealed that lower temperatures of heat treatment resulted in the presence not only of amorphous phase (Am), Ni and Ni₃P but also the metastable phases. Therefore, Ni-P-QD 60 g/l composite coating was optimum due to the distribution of the SiO₂ particles towards the substrate uniformly and excessive particles were distributed on Ni-P-QD 100 g/l effects the microhardness value.

4. CONCLUSION

In summary, the Ni-P QD 60 g/l with heat treatment at 200°C shows that successfully improved the wear resistance compared to other composite coatings. This is due to the presence of high silica and alumina content in the quarry dust particles co-deposited in the nickel matrix. Furthermore, it is also due to the phase transformation from Ni to Ni₃P after the heat treatment process.

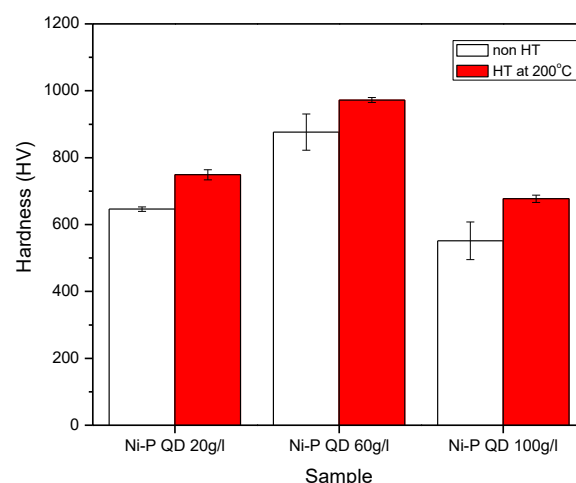


Figure 3 Microhardness of Ni-P-QD composite coatings.

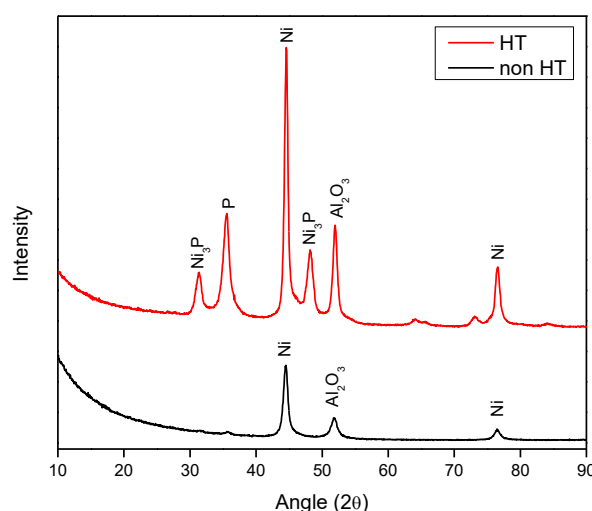


Figure 4 XRD pattern of Ni-P-QD composite coating 60g/l.

ACKNOWLEDGEMENT

We greatly acknowledge the research funding from Fundamental Research Grant Scheme (FRGS/1/2017/TK10/UTEM/03/4) and Universiti Teknikal Malaysia Melaka (UTeM) for sponsoring this work.

REFERENCES

- [1] Boothroyd, G. (1988). *Fundamentals of metal machining and machine tools* (Vol. 28). Crc Press.
- [2] Ayed, Y., Germain, G., Ammar, A., & Furet, B. (2013). Degradation modes and tool wear mechanisms in finish and rough machining of Ti17 Titanium alloy under high-pressure water jet assistance. *Wear*, 305(1-2), 228-237.
- [3] Smith, G. T. (1989). *Advanced machining: the handbook of cutting technology*. IFS.
- [4] Torabinejad, V., Rouhaghdam, A. S., Aliofkhazraei, M., & Allahyarzadeh, M. H. (2016). Electrodeposition of Ni-Fe and Ni-Fe-(nano Al₂O₃) multilayer coatings. *Journal of Alloys and Compounds*, 657, 526-536.
- [5] Jiang, S. W., Yang, L., Pang, J. N., Lin, H., & Wang, Z. Q. (2016). Electrodeposition of Ni-

- Al₂O₃ composite coatings with combined addition of SDS and HPB surfactants. *Surface and Coatings Technology*, 286, 197-205.
- [6] Liu, W. Q., Lei, W. N., Wang, C. Y., Qian, H. F., & Ding, L. H. (2015). Ni-SiC nanocomposites electroplating process under ultrasonic and agitation. *Integrated Ferroelectrics*, 167(1), 192-198.
- [7] Othman, I. S., Azhar, E. N., Azam, M. A. F. M. M., Kasim, M. S., Abidin, M. Z. Z., Sundi, S. A., & Jun, L. P. (2018). Tribological properties of malaysian quarry dust reinforced nickel matrix composite coatings. *Proceedings of Asia International Conference on Tribology 2018*, 87-89.
- [8] Keong, K. G., Sha, W., & Malinov, S. (2002). Crystallisation kinetics and phase transformation behaviour of electroless nickel-phosphorus deposits with high phosphorus content. *Journal of Alloys and Compounds*, 334(1-2), 192-199.

Surface topography study of CNC milled zirconia dental restoration

Rahimah Abdul Hamid*, Wan Nur Amirah Wan Muhamad, Raja Izamshah Raja Abdullah, Mohd. Shahir Kasim

¹⁾ Fakulti Kejuruteraan Pembuatan, Universiti Teknikal Malaysia Melaka, Hang Tuah Jaya, 76100 Durian Tunggal, Melaka, Malaysia

*Corresponding e-mail: rahimah.hamid@utem.edu.my

Keywords: Zirconia ceramic; surface structure; SEM

ABSTRACT – The aim of the study was to analyze the surface topography of computer-aided-design-computer-aided-manufacturing (CAD-CAM) milled zirconia dental restoration. The surface analysis was studied by using Scanning Electron Microscopy (SEM) machine. SEM results showed periodic surface profile of the surface structure due to the scallop-height effect. In addition, the micro-pitting was also observed. This has caused average surface roughness of 0.04-0.5 μ m of some random measurement points as a result of different stylus locations during the measurement. The improvement of the untreated surface profile could be achieved with some finishing and polishing techniques which are not considered in the present study.

1. INTRODUCTION

A complex curved surface is widely used in dental restoration with a rapidly varied geometric feature. The milling of this complex geometric feature with uniform processing parameters for the whole machining region has created the scallop-height effect on the milled restorations. The scallop-surface depends on the toolpath and the size of the cutter [1]. As a result of scallop-height formation, the milled dental restorations exhibit a variation in surface roughness which requires additional finishing and polishing of the restorations. In dentistry, the surface roughness is responsible for the microbial attractiveness of denture surfaces [2] and has to be strictly monitored. Microbial adhesion is enhanced with increasing surface roughness between 0.1 and 0.4 μ m [3], and Bollen et al. [4] stated that the *Ra* value of 0.2 μ m will not influence bacterial adhesion or colonization. Therefore, the aim of the present study was to study the surface topology of the untreated milled dental restoration and discuss the effect of this scallop-height towards its surface roughness. The testing hypothesis was that the surface roughness would be below 0.5 μ m.

2. MATERIAL AND METHOD

2.1 Experimental Set-up

Machining experiment was performed on Ardentia DT 100 milling machine under dry machining with a carbide tool. The work material used for the experiment was NexxZr T, which is dental zirconium oxide (Y-TZP ZrO₂) from Sagemax Bioceramics, Inc. The disc had undergone a sintering temperature between 1500-1530 °C.

2.2 Surface Roughness Measuring Procedure

The roughness characteristic measured was arithmetic average (*Ra*), which is determined as the

arithmetic mean of absolute values of the roughness profile ordinates that was measured using a contact-type stylus profilometer: Mitutoyo surface roughness tester. The stylus traversing length, *Lt*, was set to 0.24mm with the cut-off, λ_c , at 0.08 mm as to set the number of sampling, λ of three. The specified points were selected at the buccal and lingual area of the restoration, as shown in Fig. 1. The occlusal surface was not examined in this surface roughness measurement due to the complicated geometry profile of this region. Average surface roughness was recorded based on 3 traces of each point.

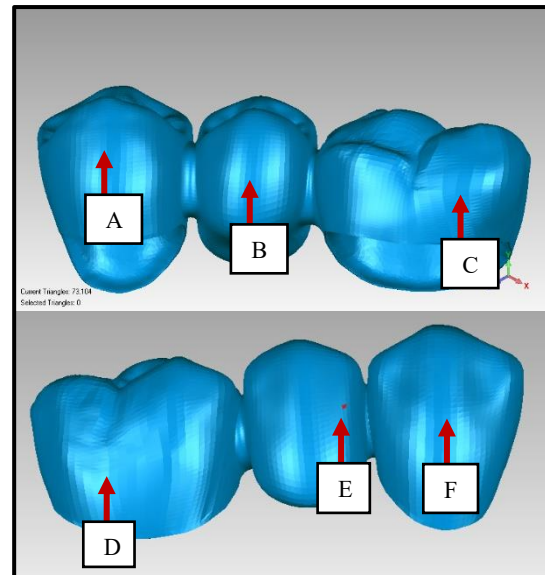


Figure 1 The measurement points.

2.3 Surface Topography Analysis

The surface structure of the milled dental restoration was analyzed using SEM machine. The purpose of this investigation was to study the surface topography of the untreated Zirconia restoration. The sample was initially sputter coated to avoid electrostatic discharge of the non-metallic sample. The surface images were captured by using Carl Zeiss Evo 50 at 15.00kV accelerating voltage for 100x and 500x of magnification power at secondary electron.

3. RESULTS AND DISCUSSION

3.1 Surface Roughness Data

The average surface roughness of each measurement point is summarized in Table 1. All specimens yielded the *Ra* values lower than 0.5 μ m, except for point F. In this study, three times of measurement were taken for each point and the average data was calculated in order to reduce the random error.

The R_a value could be improved if a greater number of traces for each point is taken, as the outlier of the reading will be eliminated so that the standard deviation, σ of each sample is less than to 0.05.

Table 1 Surface roughness data (R_a) for all points.

| Point | Reading 1 (μm) | Reading 2 (μm) | Reading 3 (μm) | Mean (μm) |
|-------|-----------------------------|-----------------------------|-----------------------------|------------------------|
| A | 0.04 | 0.03 | 0.04 | 0.037 |
| B | 0.04 | 0.04 | 0.16 | 0.08 |
| C | 0.29 | 0.38 | 0.32 | 0.33 |
| D | 0.27 | 0.28 | 0.45 | 0.33 |
| E | 0.42 | 0.55 | 0.36 | 0.44 |
| F | 0.56 | 0.34 | 0.65 | 0.52 |

According to Shahir et al. [5], the R_a values depend on the stylus location of the profilometer, as shown in Fig. 2. This could explain the variation of R_a values for each point during the multiple tracing.

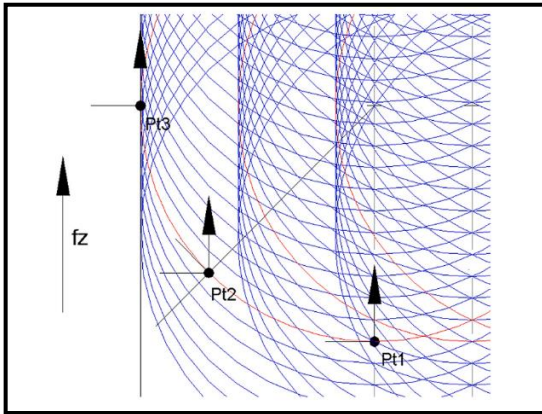


Figure 2 Schematic diagram that shows the R_a value varies depending on the stylus location [5].

3.2 Surface Topography Data

SEM images showed the scallop-height effect of the untreated surface of the milled zirconia restoration due to the cutter. The profile of the machined surface is dominated by the reflective deflection between the tool and the workpiece during machining [6]. In addition, the micro-pitting of the surface was also observed, as a result of the compaction process of zirconia-powder during the manufacturing of the ceramic disc.

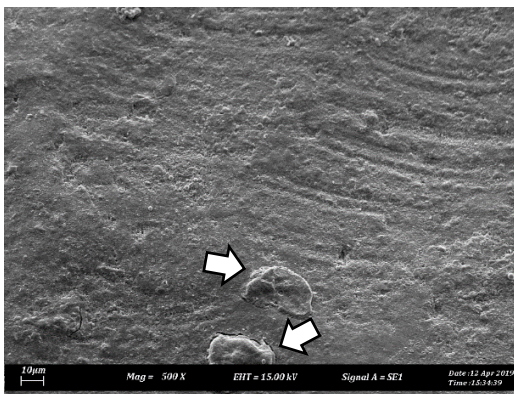


Figure 3 SEM image of the specimen (x500) with scratch grooves. The arrow indicates micro-pitting.

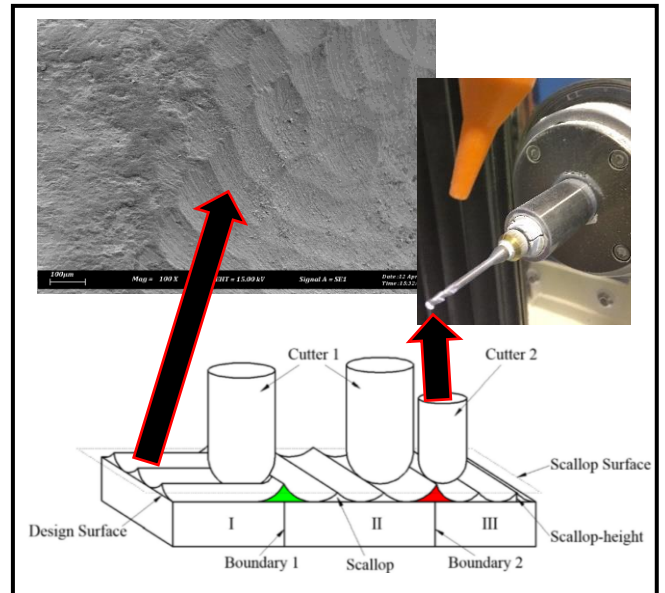


Figure 4 Illustration of scallop-height effect [1], and SEM image of the restoration (x100).

CONCLUSION

The scallop-height effect, the scratch grooves, and the micro-pitting of the surfaces contributed to the high surface roughness of the fabricated dental restoration.

ACKNOWLEDGEMENT

The authors are grateful to UTeM and the Ministry of Higher Education Malaysia for funding this research project through a grant FRGS/2018/FKP-AMC/F00378.

REFERENCES

- [1] Jia, Z. Y., Zhao, X. X., Ma, J. W., Chen, S. Y., Qin, F. Z., & Liu, Z. (2019). Toolpath generation in sub-regional processing with constraint of constant scallop-height at boundary for complex curved surface. *Precision Eng.*, 55(2019), 217–230.
- [2] Steinmassl, O., Dumfahrt, H., Grunert, I., & Steinmassl, P. A. (2018). Influence of CAD/CAM fabrication on denture surface properties. *Journal of Oral Rehabilitation.*, 45(5), 406–413.
- [3] Tamada, M., Katakai, A., Yuasa, A., Terada, A., Kushimoto, T., & Tsuneda, S. (2006). Bacterial adhesion to and viability on positively charged polymer surfaces. *Microbiology*, 152(12), 3575–3583.
- [4] Bollen, C. M. L., Papaioanno, W., Van Eldere, J., Schepers, E., Quirynen, M., & Van Steenberghe, D. (1996). The influence of abutment surface roughness on plaque accumulation and peri-implant mucositis. *Clinical Oral Implants Research*, 7(3), 201–211.
- [5] Chung, Y. J., & Jun H. O. (1991). Improvement of surface waviness by cutting force control in milling. *Int. Journal of Machine Tools and Manufacturing.*, 31(1), 9–21.
- [6] Kasim, M. S., Hafiz, M. S. A., Ghani, J. A., Haron, C. H. C., Izamshah, R., Sundi, S. A., & Othman, I. S. (2018). Investigation of surface topology in ball nose end milling process of Inconel 718. *Wear*, 426–427(Dec. 2018), 1318–1326.

The effect of coconut fibre as friction modifier on mechanical and tribological characteristics of friction materials

Hazim Sharudin^{1,*}, R.J. Talib², M. Hisyam Basri¹, N.I. Ismail¹, Arif Pahmi¹, M.F.S. Khalid³

¹⁾Faculty of Mechanical Engineering, Universiti Teknologi MARA,
Kampus Pulau Pinang, Permatang Pauh, Pulau Pinang, Malaysia

²⁾Zeta Scientific Sdn. Bhd, Blok 5, Kompleks Otomobil, 23-1B, Jalan Pahat H15/H, Seksyen 15,
40200 Shah Alam, Selangor, Malaysia

³⁾Faculty of Mechanical Engineering, Universiti Teknologi MARA Cawangan Johor,
Kampus Pasir Gudang, 81750 Masai, Johor, Malaysia

*Corresponding e-mail: hazim@uitm.edu.my

Keywords: Coconut fibres friction materials; hardness; friction and wear

ABSTRACT – The main purpose of this project is to investigate the effect of different volume percentage (vol.%) of coconut fibres on mechanical and tribological characteristics of friction materials. Four brake friction material formulations of different compositions were prepared through powder metallurgy process. All the test samples were examined for their density, porosity, hardness, thickness loss and coefficient of friction (COF) which follow the international standard test procedure. Test results obtained show that sample J2 which composed of 15% coconut fibres is the best formulation as it produced stable COF and lower thickness loss results.

1. INTRODUCTION

Brake pad friction materials is an element of the brake system used in the automotive and other applications and the friction material does its job by converting the energy of motion to heat energy through brake pads and disc. Friction materials behaviour depend on the speed, deceleration, and mode of braking; whether it is continuous or intermittent. In addition, a good friction material should compose of four components; classified as binders, reinforcements, fillers and frictional additives [1]. Friction modifier such as graphite, kenaf, iron oxide is used to improve the coefficient of friction (COF) and wear properties of the brake friction materials. It is important to note that certain material content in the friction material composition perform multiple functions includes stable friction, adequate wear resistance and improved fade.

In order to obtain reliable brake performance, some modifications need to be made on the formulations and several methodologies on the formulation of frictional material have been reported [2,3]. All the proper formulations for optimum brake performance were obtained by undergoing different design of experiments. Besides the friction modifier that has been stated before, coconut fibres are one of the natural fibres that provide excellent insulation against temperature, unaffected by moisture and dampness, most ductile and energy absorbent material. Thus, coconut fibres appeared to be suitable to use as a base material in friction material [4]. This work investigates the compatibility of coconut fibres as friction modifier in the fabrication of brake friction materials.

2. METHODOLOGY

2.1 Test Samples Preparation

Four types of brake friction material formulations have been prepared after undergoing powder metallurgy process. Firstly, the composition were mixed together in the tubular mixer with the speed and timer were adjusted to 50 rpm and 10 minutes of mixing time. All the test samples then were warm compacted by using SANTEC Hydraulic Hot Press Machine under a pressure of 15 tonne at a temperature of 170°C for 4 minutes. In order to improve the dimensional stability and improve compressive creep resistance, the compacted test samples were post-baked at a temperature of 200°C for 4 hours, in an oven. Table 1 shows all the test samples consists of coconut fibre and other composition at the volume percentages (vol %).

Table 1 Samples composition.

| Composition | J1 | J2 | J3 | J4 |
|---------------|------|------|------|------|
| Coconut Fibre | 10.0 | 15.0 | 5.0 | 7.9 |
| Resin | 15.0 | 14.1 | 15.9 | 11.8 |
| Graphite | 15.0 | 14.1 | 15.9 | 11.8 |
| Steel Fibre | 30.0 | 28.4 | 31.6 | 45.0 |
| Iron Powder | 20.0 | 18.9 | 21.1 | 15.8 |
| Copper | 10.0 | 9.5 | 10.5 | 7.9 |
| Total (vol %) | 100 | 100 | 100 | 100 |

2.2 Testing and Analysis

All the four test samples were tested for the Rockwell hardness and porosity tests in accordance to currents available test standard which are MS 474: Part 2 and JIS D 4418. In terms of friction and wear tests, it was performed using CHASE dynamometer and the test procedure was accordance to the SAE J616 standard. The test was carried out by pressing the sample against rotating brake drum under a constant load of 647 N and constant rotating speed of 417 rpm. Further explanation of the test program can be referred in the previous publication [3].

3. RESULTS AND DISCUSSION

Table 2 shows the effects of coconut fibers on the material properties (density, hardness and porosity) of the developed brake friction materials. It indicates that the coconut fibers significantly increase hardness, while in the case of porosity, the effect is opposite. Based on these

results, it was noted that there is no direct correlation between vol.% of coconut fibers with the mechanical properties as well as the correlation between porosity with the hardness behavior. This is because, the hardness increase with coconut fibers is attributed to good bonding as well as due to the high hardness of the thermosetting binder resin after cure [3]. On the other hand, coconut fibers decrease porosity for sample J2 and J3 because it flows through gaps inside the friction material during hot pressing process and fills voids before it is combined during curing. As the vol.% of coconut fibers decreases from J2 until J4, the density is increasing due to the difference in formulations and also the factor of post-baking the brake pad as it changes the structure of material in the friction materials.

Table 2 Samples test results.

| Sample | Density (g/cm ³) | Hardness (Shore D) | Porosity (%) |
|--------|------------------------------|--------------------|--------------|
| J1 | 2.734 | 89.50 | 27.63 |
| J2 | 2.421 | 19.70 | 23.56 |
| J3 | 2.708 | 41.77 | 21.31 |
| J4 | 2.717 | 77.03 | 29.13 |

Figure 1 shows the Coefficient of Friction (COF) increased with increasing temperature for all the four samples. Beginning of braking, the harder asperities on the brake disc being ploughed into the wear surface and widening the contact area of the brake pad which making the COF increased. Thereafter, the degradation of the coconut fibers causes the mechanical integrity of formulation to become gradually weaker that makes the COF decreased. The shearing of the peak asperities and formation of friction film could also reduce the COF as observed by other researchers [4]. Sample J4 which composed of 7.9 vol.% coconut fibers has the lowest COF. This is could be due to the decomposition of coconut fibers at elevated temperature resulting the lower bonding of the composition. It can be seen from Figure 1 that sample J2 showed an excellent fade resistance and more stable COF compared to sample J3 and J4.

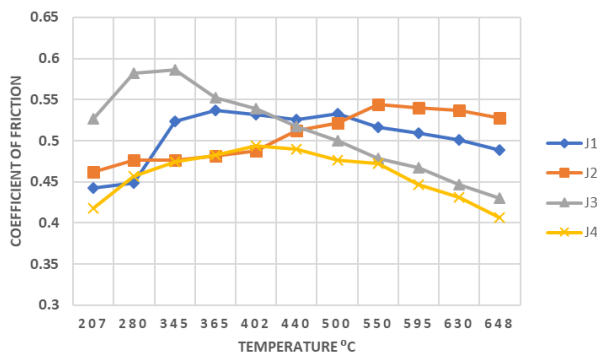


Figure 1 COF characteristics of different vol% of coconut fibers in the formulations.

Figure 2 shows that sample J1 which composed of 10 vol.% of coconut fibers has the lowest thickness loss while sample J3 which composed of 5 vol.% of coconut fibers has the highest thickness loss. Decrement in vol. % of coconut fibers would result a higher thickness loss, thus increase weight loss of the sample. This

phenomenon could be due to increase in hardness and reduction in porosity with respect of vol.% coconut fibers in the formulation. In addition, it is observed that there is no direct correlation between vol.% coconut fibers with the thickness loss during braking because other parameter such as wear mechanism and mode of braking might influence the thickness loss [4].

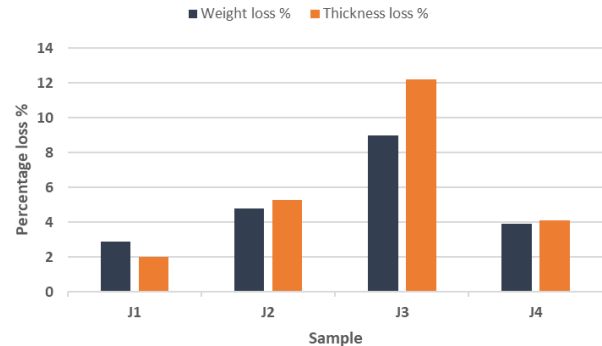


Figure 2 Thickness loss characteristics of different vol. % of coconut fibers in the formulation.

4. CONCLUSION

It can be concluded that coconut fibres improves the mechanical and tribological properties of friction materials in which the porosity decrease and the thickness loss increase with decreasing of vol. % of coconut fibres in the formulation. Sample J2 which composed of 15 vol. % of coconut fibres is the best formulation which produced on stable COF and lower thickness loss results.

ACKNOWLEDGMENT

The authors would like to thank Universiti Teknologi MARA Cawangan Pulau Pinang and AMREC, SIRIM Berhad for the support and providing characterisation equipments and the research facilities.

REFERENCES

- [1] N. A. Norrdin, R. J. Talib, R. Rabilah, Hazim Sharudin, N. N. Azmi, S. N. A. M. Halidi, & N. S. Abdullah. (2018). Influence of resin on mechanical and tribological properties of friction materials. *Proceedings of Asia International Conference on Tribology 2018*, 489-490.
- [2] Zaharudin, A. M., Berhan, M. N., & Talib, R. J. (2011). The effect of phenolic resin, rubber, calcium carbonate and graphite on tribological characteristic of semi-metallic brake. *AIP Conference Proceedings*, 1400(1), 274-279.
- [3] Almaslow, A., Ratnam, C. T., Ghazali, M. J., Talib, R. J., & Azhari, C. H. (2013). Effects of electron-beam and sulfur crosslinking of epoxidized natural rubber on the friction performance of semimetallic friction materials. *Composites Part B: Engineering*, 54, 377-382.
- [4] Jaafar, T. R., Othman, E. A., Selamat, M. A., & Kasiran, R. (2016). On-road braking performances of semi-metallics brake friction materials developed through powder metallurgy process. *Journal of Engineering Science*, 12, 27-41.

Adhesion modelling for load-dependence, double-Hertz based elliptical contacts

Nurul Hilwa Mohd Zini^{1,2,*}, Matthijn de Rooij³, Mohammad Bazrafshan³, Aydar Akchurin³, Dik Schipper³, Nurhidayah Ismail^{1,2}

¹⁾Fakulti Kejuruteraan Mekanikal, Universiti Teknikal Malaysia Melaka, Hang Tuah Jaya, 76100 Durian Tunggal, Melaka, Malaysia

²⁾Centre for Advanced Research on Energy, Universiti Teknikal Malaysia Melaka, Hang Tuah Jaya, 76100 Durian Tunggal, Melaka, Malaysia

³⁾Department of Surface Technology and Tribology, Faculty of Engineering Technology, University of Twente, the Netherlands

*Corresponding e-mail: nurulhilwa@utem.edu.my

Keywords: Double-Hertz model; elliptical contact; pull-off force

ABSTRACT – The recently developed Double-Hertz (DH) model for adhesive elliptical contacts is shown to be suitable only for nearly circular contacts; this is due to the geometry of the adhesive region is unknown a priori. To solve this problem, the geometry of the adhesive region at the pull-off moment is predicted numerically using the Boundary Element Method and the data is then used to curve-fit equations of the ellipticity ratio and the semi-major axis of the elliptical area. The resulting equations can then be incorporated into the extended DH model for accurate pull-off force predictions.

1. INTRODUCTION

The Double-Hertz model for adhesive contacts has been extended recently in [1] to describe adhesion between two cylindrical bodies that cross each other at a skew angle, θ_{skew} ranging between 0 to 90 degrees. The resulting adhesive region is shown in Figure 1.

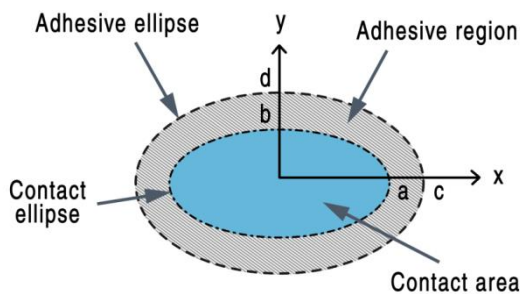


Figure 1 Adhesive region of a DH-based elliptical contact [2].

Although the load effect on boundary of the adhesive regions during contact is recognized in [1] as the correct geometrical behaviour for the DH based adhesive region, analytical solutions that can be used to calculate the ellipticity ratios for contact and adhesive ellipses, β_{ab} and β_{cd} at the pull-off force moment are unavailable. This limits the application of the DH elliptical model to nearly circular contacts ($\theta_{skew} \approx 90^\circ$). Thus, to ensure that the DH elliptical model can predict accurately other contacts with lower θ_{skew} , a numerical solution becomes necessary to accurately predict both β_{ab} and β_{cd} values, for a wide range of adhesive elliptical contacts.

2. ADHESIVE CONTACT MODELLING

The development of the extended DH model in [1] is continued for adhesive elliptical contacts with lower θ_{skew} , with a new assumption which the adhesive region is allowed to change without the constraint of a Hertzian contact. Both β_{ab} and β_{cd} that act as the inner and the outer boundaries of the adhesive region have ellipticity ratios that vary with load, with both having similar values of ellipticity ratio at the beginning of the contact. As the contact progresses to the pull-off force moment, both boundaries begin to change in size, with the inner boundary having a different ellipticity ratio compared to the outer boundary, though both boundaries are assumed to maintain their elliptical shapes.

In this work, the adhesive region is assumed to be load-dependent hence at the pull-off moment both, β_{ab} and β_{cd} can be expressed as:

$$\beta_{ab} = \beta_{ab_{pull-off}} \quad (1a)$$

$$\beta_{cd} = \beta_{cd_{pull-off}} \quad (1b)$$

β_{Hertz} is the constant ellipticity ratio obtained from a normal elliptical Hertzian contact while β_0 is the initial ellipticity ratio at the beginning of the adhesive contact. Before the ellipticity ratio changes due to the applied load, the assumption for the adhesive contact at the initial load can be summarized as:

$$\beta_0 = \beta_{0ab} = \beta_{0cd} \quad (2a)$$

$$\beta_0 = \beta_{Hertz} \quad (2b)$$

where β_{0ab} and β_{0cd} are the initial ellipticity ratios for the contact and adhesive ellipses, respectively. Assumptions in Equation (2) are made to approximate the behaviour for both contact and adhesive ellipses; though these assumptions are more suitable for 'rigid' materials with low value of Tabor parameter, μ .

The geometry of DH based adhesive regions due to elliptical contacts can be simulated by a Boundary Element Model (BEM) with a Dugdale approximation for the adhesive stress, developed by [3]. The developed numerical model utilizes the Conjugate Gradient Method (CGM). The numerical model is suitable to solve non-linear contact problems such as adhesive elliptical contacts where the contact geometry is unknown a priori. In the method, the contribution of each element in the pressure and the deformation profiles is considered separately. The CGM algorithm is shown in Figure 2.

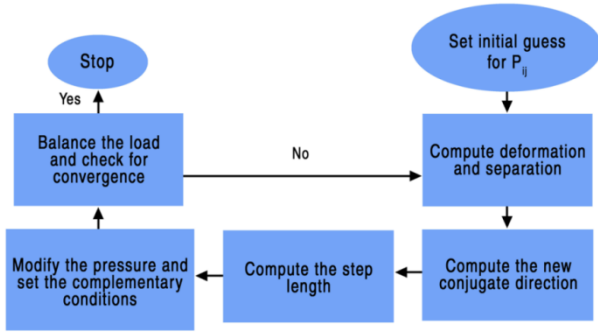


Figure 2 CGM based algorithm for adhesive contacts [3].

Numerical simulations are conducted for various β_0 values of 0.3 ($\theta_{skew} = 43.63^\circ$), 0.4 ($\theta_{skew} = 53.14^\circ$), 0.6 ($\theta_{skew} = 68.51^\circ$) and 0.8 ($\theta_{skew} = 80.45^\circ$), within the range of $0.5 \leq \mu \leq 4$. Results from the numerical simulations are obtained using a minimum element number of $N = 2048$ for $0.5 \leq \mu < 2$ (the domain size is 2048×2048 elements) and a maximum element number of $N = 4096$ for $2 \leq \mu \leq 4$ (the domain size is 4096×4096 elements). In all cases, the calculation domain is set six times greater than the contact domain. An increased resolution is required for larger μ values due to the small adhesive zone outside the contact. The accurate prediction of β_{ab} and β_{cd} values at the pull-off moment uses a negative load input in the numerical algorithm; this negative load represents the pull-off force required to separate the contacting surfaces. The pull-off force is determined by the greatest negative load that first converges within 200 iterations.

3. RESULTS AND DISCUSSION

An example of the numerical model's results on predicting adhesive elliptical contacts at the pull-off moment are shown in Figure 3. The results are obtained using the contact parameters in Table 1 as the input. Figure 3a shows the image of a three-dimensional pressure profile within the computation domain with 2048 elements along the semi-major and semi-minor axes while Figure 3b and Figure 3c show the resulting pressure distribution along the semi-major axis and semi-minor axis. The selected points of a and b are obtained from the semi-major and semi-minor axes of the contact ellipse while the points of c and d are obtained from the semi-major and semi-minor axes of the adhesive ellipse.

Table 1 Parameter of the adhesive elliptical contact at the pull-off moment.

| Parameters | Values | Unit |
|---------------------------------------|--------|---------------|
| Predicted pull-off force | 75 | nN |
| Fiber diameter | 3.5 | μm |
| Skew angle, θ_{skew} | 43.63 | $^\circ$ |
| Hertzian ellipticity ratio, β_0 | 0.3 | - |
| Tabor parameter, μ | 0.5 | - |
| Number of elements, N | 2048 | - |

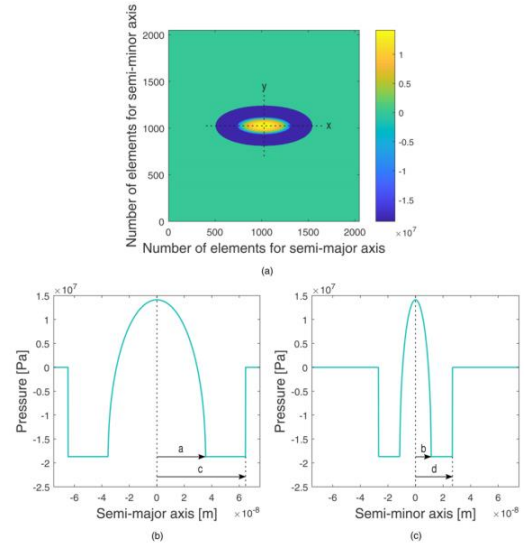


Figure 3 Numerical solutions for the elliptical contact (a) pressure profile for the elliptical contact (b) stress distribution along the semi-major axis and (c) stress distribution along the semi-minor axis.

Using the data from the numerical model, we have obtained the equations that can predict the values of β_{ab} and β_{cd} at the pull-off moment, as a function of μ and θ_{skew} . These ellipticity ratio equations at the pull-off moment are given as:

$$\beta_{ab} = 0.389\theta_{skew}^{1.767} + 0.083\mu^{0.332} + 0.023 \quad (3a)$$

$$\beta_{cd} = 0.414\theta_{skew}^{1.584} + 0.72\mu^{-0.007} - 0.578 \quad (3b)$$

The equation to predict the semi-major axis of the contact ellipse at the pull-off moment, a is given as:

$$a = \left(\frac{R^2 \Delta \gamma}{E^*} \right)^{1/3} \left(\sinh(1.05\beta_{ab}^{-0.16} - 0.065\mu^{-1.2}) \right)^2 \quad (4)$$

Equation (3) and (4) can then be incorporated into the extended DH model to predict the elliptical contacts.

4. SUMMARY

The work on the extended DH model has been continued to include the assumption of an adhesive region with boundaries that vary with load. The resulting curve-fitted equations for the geometry of the adhesive regions obtained numerically can be incorporated into the extended DH model for an accurate pull-off prediction of elliptical contacts.

REFERENCES

- [1] Zini, N.H.M., de Rooij, M.B., Bazrafshan, M., Ismail, N., Schipper, D.J. (2018). Extending the double-Hertz model to allow modeling of an adhesive elliptical contact. *Tribology Letters*, 66(1), 30-43.
- [2] Zini, N.H.M., de Rooij, M.B., Bazrafshan, M., Ismail, N., Schipper, D.J. (2018). Response to Dr. Greenwood's comments on "Extending the double-Hertz model to allow modeling of an adhesive elliptical contact". *Tribology Letters*, 66(9), 99.
- [3] Bazrafshan, M., de Rooij, M.B., Valefi, M., Schipper, D.J. (2017). Numerical method for the adhesive normal contact analysis based on a Dugdale approximation. *Tribology International*, 112(8), 117-128.